DOT/FAA/TC-19/41, P2

Federal Aviation Administration
William J. Hughes Technical Center
Aviation Research Division
Atlantic City International Airport
New Jersey 08405

Aluminum 2024-T351 Input Parameters for *MAT_224 in LS-DYNA

Part 2: Additional tests to determine plastic heating and ductile fracture behavior under combined loading

August, 2022

Final report

U.S. Department of Transportation
Federal Aviation Administration

NOTICE

This report is available at the Federal Aviation Administration William J. Hughes Technical Center's Full-Text Technical Reports page: actlibrary.tc.faa.gov in Adobe Acrobat portable document format (PDF).

Form DOT F 1700.7 (8-72) Reproduction of completed page authorized

1. Report No.	2. Government Accession No.	3. Recipient's Catalog No.
DOT/FAA/TC-19/41, P2		

4. Title and Subtitle	5. Report Date
Title of Report: Aluminum 2024-T351 Input Parameters for *MAT_224 in LS-DYNA, Part 2: Additional tests to determine plastic heating and ductile fracture behavior under combined loading	August 2022
	6. Performing Organization Code
7. Author(s)	8. Performing Organization Report No.
Seidt, J.D., Smith, J.L, Spulak, N., Lowe, R.L., Gilat, A.	
9. Performing Organization Name and Address	10. Work Unit No. (TRAIS)
The Ohio State University, Dynamic Mechanics of Materials Laboratory (DMML) 201 West 19th Ave. Columbus, OH 43210	
	11. Contract or Grant No. 16-G-007
12. Sponsoring Agency Name and Address	13. Type of Report and Period Covered
U.S. Department of Transportation Federal Aviation Administration Air Traffic Organization Operations Planning Office of Aviation Research and Development Washington, DC 20591	Final Report
	14. Sponsoring Agency Code AIR-6A1

15. Supplementary Notes

The Federal Aviation Administration William J. Hughes Technical Center Aviation Research Division Technical Monitor was Daniel Cordasco.

16. Abstract

A team consisting of The Ohio State University (OSU), George Mason University (GMU), National Aeronautics and Space Administration Glenn Research Center (NASA-GRC), and the Federal Aviation Administration (FAA) Aircraft Catastrophic Failure Prevention Research Program (ACFPP) collaborated to develop a new material model in LS-DYNA for Aluminum 2024-T351. An initial set of reports were produced as DOT/FAA/AR-13/25 P1-3. This supplemental report describes additional experiments designed and conducted to answer questions that arose during the *MAT_224 card development process. The additional tests were organized into three groups: 1) Dynamic tension tests to study the conversion of plastic work into heat at high strain rates, 2) tests conducted to determine the fracture strain of 2024-T351 aluminum under a specific state of compression and shear, and 3) tests conducted to determine the material fracture strain under a certain three-dimensional stress state (in-plane biaxial tension and through thickness compression). To study conversion of plastic work to heat, tension tests on miniature dog-bone coupons were conducted at strain rates ranging from 1E-4 s-1 to 6000 s-1. During the tests, full-field strain and temperature were measured on opposite sides of the sample using high speed Digital Image Correlation (DIC) and a Telops high speed thermal infrared (IR) camera, respectively. Both strain and temperature data were superposed on a common coordinate system using MATLAB-based image processing techniques; average Taylor-Quinney (Beta) parameters were then determined. To further characterize the fracture strain dependence on stress state, an additional stress state was measured via a combined compression and shear (torsion) test using an axial-torsional hydraulic load frame. The new stress state had the highest ratio of compressive to torsional stress tested to date. To study the effect of the in-plane biaxial tension plus through thickness compression on the fracture strain of Aluminum 2024-T35, a new punch test with a backing plate was designed and conducted. These new tests were based on ASTM E643-15 Standard Test Method for Ball Punch Deformation of Metallic Sheet Material. The standard tests were modified such that the ratio of the die diameter to the punch diameter was dramatically increased and in two cases, a ductile copper backing plate was added behind the aluminum test specimen, providing out-of-plane compression. Three types of tests were conducted: 1) unbacked, 2) backed test with thin copper plate and 3) backed test with thick copper plate. These tests were designed to ensure that the stress triaxiality ranged from -2/3 to 0.113 while maintaining a near constant Lode parameter of -1. Tests conducted for backed experiments included both monotonic tests to failure and sequential loading-unloading tests to analyze strain evolution and failure morphology. Fracture strains for the backed experiments were determined to be substantially higher than those from unbacked (biaxial tension only) tests.

17. Key Words	18. Distribution Statement
plastic deformation, fracture, strain rate sensitivity, temperature sensitivity, stress state dependence, split Hopkinson bar, Digital Image Correlation, Aluminum 2024, *MAT_224	This document is available to the U.S. public through the National Technical Information Service (NTIS), Springfield, Virginia 22161. This document is also available from the Federal Aviation Administration William J. Hughes Technical Center at actlibrary.tc.faa.gov.

19. Security Classif. (of this report)	20. Security Classif. (of this page)	21. No. of Pages	19. Security Classif. (of this report)
Unclassified	Unclassified	59	Unclassified

ACKNOWLEDGEMENTS

This research was funded by the Federal Aviation Administration's (FAA's) Aircraft Catastrophic Failure Prevention Program (ACFPP) under aviation research grant 16-G-007. Thanks to Don Altobelli, Bill Emmerling, Dan Cordasco and Chip Queitzsch who oversaw a remarkable team of researchers for this project. Thanks to Mike Pereira, Kelly Carney, Duane Revilock, Chuck Ruggeri and Brad Lerch of NASA Glenn Research Center. Thanks also to Paul Dubois, Jeanne He, Steve Kan, Murat Buyuk.

Contents

Figures

Tables

Acronyms

Acronym	Definition
ACFPP	Aircraft Catastrophic Failure Prevention Program
ASTM	American Society for Testing and Materials
DIC	Digital Image Correlation
DMML	Dynamic Mechanics of Materials Laboratory (OSU)
DOT	Department of Transportation
EDM	Electric Discharge Machine
FAA	Federal Aviation Administration
FLIR	Forward-looking InfraRed
fps	frames per second
GMU	George Mason University
GRC	Glenn Research Center (NASA)
IR	Infrared
NASA	National Aeronautics and Space Administration
OSU	The Ohio State University
SHB	split Hopkinson bar
TRIP	TRansformation Induced Plasticity

Executive summary

A team consisting of The Ohio State University (OSU), The George Mason University (GMU) and National Aeronautics and Space Administration Glenn Research Center (NASA-GRC), and Federal Aviation Administration (FAA) Aircraft Catastrophic Failure Prevention Research Program collaborated to develop a new material model in LS-DYNA for Aluminum 2024-T351 with the goal of improving numerical modeling of turbine engine blade-out events. An initial set of reports were produced as DOT/FAA/AR-13/25 P1-3 (Emmerling, Altobelli, Carney, & Pereira, 2014; Buyuk, 2014; Seidt, 2014). This supplemental report describes additional experiments designed and conducted to answer questions that arose during the *MAT_224 card development for Aluminum 2024. The additional tests were organized into three groups: 1) dynamic tension tests to study the conversion of plastic work into heat at high strain rates, 2) tests conducted to determine the fracture strain of 2024-T351 aluminum under a specific state of compression and shear, and 3) tests conducted to determine the material fracture strain under a certain three- dimensional stress state (in-plane biaxial tension and through thickness compression). To study conversion of plastic work to heat, tension tests on miniature dog-bone coupons were conducted at strain rates ranging from 1E-4 s^{-1} to 6000 s^{-1}. During the tests, full-field strain and temperature were measured (on opposite sides of the sample) using high speed Digital Image Correlation (DIC) and a Telops high speed thermal infrared (IR) camera, respectively. Both strain and temperature data were superposed on a common coordinate system using MATLAB-based image processing techniques; average Taylor-Quinney (Beta) parameters were determined. To further characterize the fracture strain dependence on stress state and additional stress state was tested using a combined compression and shear (torsion) test using an axial-torsional hydraulic load frame. This new stress state had the highest ratio of compressive to torsional stress tested to date. To study the effect of the in-plane biaxial tension plus through thickness compression on the fracture strain of 2024-T351 aluminum, a new punch test based on ASTM E643-09 Standard Test Method Ball Punch Deformation of Metallic Sheet Material was designed and conducted. . The standard tests were modified to dramatically increase the ratio of the die diameter to the punch diameter and in two cases, a ductile copper backing plate was added behind the aluminum test specimen, providing out of plane compression. Three types of tests were conducted: 1) unbacked, 2) backed test with thin copper plate, and 3) backed test with thick copper plate. These tests were designed to ensure that the stress triaxiality ranged from -2/3

to 0.113 while maintaining a near constant Lode parameter of -1. For backed experiments, both monotonic tests to failure and sequential loading-unloading tests to analyze strain evolution and failure morphology were conducted. Fracture strains for the backed experiments were determined to be substantially higher than those from unbacked (biaxial tension only) tests.

1 Introduction

This report, a supplement to DOT/FAA report TC-19/41 P1 (Park, Kelly, DuBois, Condasco, & Kan, 2020), describes additional experiments designed and conducted to answer questions that arose during the *MAT_224 card development for 2024-T351 aluminum plate. The tests in this report are organized into three groups: 1) additional dynamic tension tests to study the conversion of plastic work into heat at high strain rates, 2) additional tests conducted to determine the fracture strain of 2024-T351 aluminum under a specific state of compression and shear and 3) additional tests conducted to determine the material fracture strain under a certain three-dimensional stress state (in-plane biaxial tension and through thickness compression). To study conversion of plastic work to heat, tension tests on miniature dog-bone coupons were conducted at strain rates ranging from 1E-4 s^{-1} to 6000 s^{-1}. During the tests, full-field strain and temperature were measured (on opposite sides of the sample) using high speed Digital Image Correlation (DIC) and a Telops high speed thermal IR camera, respectively. Both strain and temperature data are superposed on a common coordinate system using MATLAB-based image processing techniques and average Taylor-Quinney (Beta) parameters were determined. To further characterize the fracture strain dependence on stress state and additional stress state was tested using a combined compression and shear (torsion) test using an axial-torsional hydraulic load frame. This new stress state has the highest ratio of compressive to torsional stress tested to date. To study the effect of the in-plane biaxial tension plus through thickness compression on the fracture strain of 2024-T351 aluminum, a new punch test with a backing plate was designed and conducted. These new tests are based on ASTM E643-09 Standard Test Method for Ball Punch Deformation of Metallic Sheet Material (ASTM, 2009) . The standard tests are modified such that the ratio of the die diameter to the punch diameter is dramatically increased and in two cases, a ductile copper backing plate is added behind the aluminum test specimen, providing out of plane compression. Three types of tests were conducted: 1) unbacked, 2) backed test with thin copper plate and 3) backed test with thick copper plate. These tests were designed to ensure that the stress triaxiality ranged from -2/3 to 0.113 while maintaining a near constant Lode parameter of -1. Experiments conducted using backing included both monotonic tests to failure and sequential loading-unloading tests to analyze strain evolution and failure morphology.

1.1 Background of conversion of plastic work into heat

The conversion of plastic work into heat is a very important topic of study. It is widely known that rapid accumulation of plastic strain is accompanied by large increases in material temperature. In fact, constitutive and failure models employed for decades to simulate dynamic applications have incorporated thermal softening in addition to strain rate sensitivity; (Johnson & Cook, 1983; Johnson & Cook, 1985). In the past, test series have been conducted on samples over a wide range of strain rates to determine *the rate sensitivity only* of the material. In hindsight, this is an impossible task because for every ductile material subjected to dynamic loading, *heat generation (increased material temperature) accompanies plastic deformation*. Therefore, *there is an interplay between rate and thermal sensitivity: strain rate hardening vs thermal softening.* It is impossible to determine the real effect of strain rate on the flow stress of a material if the temperature increase of the material is unmeasured. The supplemental test series detailed in this report were conducted to shed some light on this issue for 2024-T351 aluminum: a) to determine the minimum strain rate at which material temperature rise is significant and to b) determine the fraction of plastic work that is converted to heat (temperature rise) over a wide range of strain rates up to 6000 s^{-1}. Prior to this test series, all dynamic tension tests were conducted on the tension split Hopkinson Bar (SHB) apparatus without full-field DIC strain measurements. In addition to providing IR temperature data, the full-field DIC measurements provide important information about the strain gradient at the necking, eventual failure location, and the local strain rate.

Several researchers have studied the conversion of plastic work into heat. The first attempts to quantify the fraction of plastic work stored as cold work versus released as heat were conducted by Farren and Taylor (1925) and Quinney and Taylor (1934). In these experiments, large torsional plastic strains were induced in mild steel, pure iron, and copper rods using a geared torsional apparatus. The temperature of each rod was recorded with a thermocouple on the surface of each sample and with a calorimeter immediately following the loading. From these tests they concluded that the fraction of plastic work converted to heat was greater than or equal to 0.85. They also concluded that the fraction of work converted to heat was nearly constant for copper and mild steel over a range of strains. For many years following these experiments, β was assumed to be a constant value between 0.85 and 1, and insensitive to strain and strain rate. A review of similar experiments is thoroughly explored in Bever et al. (1973).

Mason et al. (1994) performed the first attempt to quantify the dependence of β on strain and strain rate in Aluminum 2024, 4340 steel and Ti-6Al-4V using a compression Kolsky bar and a high speed IR detector first designed to measure temperatures in a propagating crack by Zehnder & Rosakis (1991). The detector consisted of 8 individual InSb sensors sensitive to radiation with wavelengths from 1 to 5.5 μm and operated with a sampling rate of 2 MHz. The detectors were calibrated by placing the specimen in the experimental apparatus and simultaneously measuring the temperature of the sample and the voltage output of the sensor. Specimens of Aluminum 2024, 4340 steel, and Ti-6Al-4V were tested to failure at strain rates from 1000 to 3000 s^{-1}. The values of β obtained for Aluminum 2024 and 4340 steel calculated to be 0.85 matching earlier low strain rate tests (Mason, Rosakis, & Ravichandran, 1994) which means β is not rate sensitive for these materials. Ti-6Al-4V showed signs of strain sensitivity as β increased from 0.65 at 3% strain to 0.95 at a strain of 5% then decreased to 0.5 at a strain of 18%. The measured temperature values from the 4340 steel test revealed that the temperature field on the surface of each specimen were inhomogeneous, which called into question the strain energy measurement for the calculation of β. Utilizing the same IR detector, Hodowany (Hodowany & Ravichandran, 2000) performed compression tests on Aluminum 2024 and alpha-Titanium. In each test it was assumed the specimen experienced homogeneous deformation, uniform temperature distribution, adiabatic behavior, and negligible thermoelastic heating. Aluminum 2024 was found to be strain-dependent as β increased from 0.3 to 1 during plastic deformation from 2% to 55% plastic strain.

It is important to mention that these calculations of β are defined as β_{diff} which differs from another calculation of β known as β_{int}. This difference in β calculation was first noted by Rittel (Rittel, On the conversion of plastic work to heat during high strain rate deformation of glassy polymers, 1999) and is described by the following equations: $\beta_{int} = \frac{\rho c_p \Delta T}{\int_0^t W_p}$ (1) or $\beta_{diff} = \frac{\rho c_p \dot{T}}{d\dot{W}_p}$ (2) where ρ is the density of the material, c_p is the specific heat of the material, ΔT is the change in temperature, $\dot{T}$ is the rate of the change in temperature, $\int_0^t W_p$ is the plastic work and $d\dot{W}_p$ is the rate mechanical power. β_{int} is a relation of the thermal dissipation to mechanical work and requires simultaneous strain and temperature measurements. β_{diff} is the ratio of the rate of thermal dissipation to mechanical power and is calculated from the derivatives of the best fit curves of the plastic work and temperature data.

Several other researchers have used similar methods to determine the fraction of plastic work converted to heat in metals during high strain rate deformation assuming adiabatic conditions. Nemat-Nasser and Kapoor (1998) calculated the temperature rise in compression tests of Ta-2.5% W alloy, pure Titanium, 1018 steel, 6061 aluminum, and OFHC copper at strain rates of 3000 s^{-1}. The temperature increase was determined with a 2 mm InSb sensor divided into four separate quadrants connected to a 1MHz amplifier. Errors in temperature measurement on the surface of the specimen due to the curve of the surface or the roughness caused by plastic deformation were assumed to be negligible. β_{int} for the various materials were calculated to range from 0.6 to 0.85 but strain and strain rate sensitivity was not investigated.

Macdougall and Harding (1998) measured β_{diff} in torsion tests of Ti-6Al-4V and also measured the surface temperature of tension tests at strain rates on the order of 1000 s^{-1}. Temperatures were measured using a 12-element Hg-Cd-Te radiometer sensitive to radiation in the range of 2 to 5.5 μm. The researchers used a calibration method similar to Mason et al. (1994) and Hodowany and Ravichandran (2000), but found test material temperatures to be underestimated. Macdougall (2000) created a new calibration system that removed extraneous sources of radiation and allowed the temperature of the specimen to be more closely monitored and controlled. Using the new calibration method, Macdougall found the β_{diff} in the torsion tests increased from 0.6 at 2% strain to 0.9 at 5% strain and remained at 0.9 up to 30% strain. β_{diff} values were not calculated for the tension tests as the strain in the necking region of the specimen could not be properly evaluated.

More recently, Rittel et al. (2017) studied β_{int} for Ti-6Al-4V, Aluminum 2024 and 5086, SS 304L, 1020 steel and C300 in compression, tension and shear at strain rates ranging from 1200 to 7000 s^{-1}. The β_{int} for Ti-6Al-4V was strain dependent as β_{int} decreased from 0.5 to 0.38 with strains from 2 to 35%. Similarly, Aluminum 2024 was slightly strain dependent as β_{int} decreased from 0.4 at a strain of 5% to 0.25 at a strain of 10% strain and then remained constant at 0.25 up to a strain of 30%. Neither material was strain rate or loading mode dependent. β_{int} in tension could only be calculated from strains of 2% to 7% because the determination of the strain energy from the engineering stress and strain is no longer valid once homogeneous deformation ends and necking begins.

Simultaneous temperature and DIC measurements have been recorded by multiple researchers at low strain rates; (Saai, Louche, Tabourot, & Chang, 2010; Oliferuk, Maj, & Zembrzycki, 2015; Eisenlohr, Gutierrez-Urrutia, & Raabe, 2012; Rodríguez-Martínez, Pesci, & Rusinek, 2011; Knysh & Korkolis, 2015; Charkaluk, Seghir, Bodelot, Witz, & Dufrénoy, 2015; Yagoubi, Lamon, Batsale, Dhote, & Flem, 2015; Dumoulin, Louche, Hopperstad, & Børvik, 2010); but only two of these researchers investigated the partition of plastic work converted to heat. Knysh and Korkolis (2015) tested slender rods of 303 and 316 stainless steel, commercially pure titanium, and Ti-6Al-4V inside a thermally isolated vacuum tube with well-defined thermal boundary conditions to emulate a simple 1D heat transfer model. 2D DIC images were taken on one side of the specimen with a single 2MP camera while IR images were captured simultaneously with a Forward-looking infrared (FLIR) SC-645 camera capable of detecting temperature from -20ºC to 150ºC at a spatial resolution of 640x480 pixels. The FLIR camera viewed the specimen through a potassium bromide window allowing all relevant infrared wavelengths to be visible to the camera. Tests were conducted at strain rates from 0.001 to 0.01 s^{-1} meaning tests were not adiabatic in nature. Using the 1D heat transfer model the heat generated from deformation was isolated from the heating caused by conduction in the rod. It was found that β_{int} is not constant with the plastic strain, instead it drops as the plastic deformation accumulates. In most cases β_{int} varied between 0.55 and 0.8. All four metals exhibited strain rate dependency as β_{int} increased with increasing strain rate although the stainless steels were less strain rate dependent.

Duomoulin et al. (2010) measured the displacement and temperature fields in three different TRIP steels during tensile loading tests at a strain rate of 1.7E-3 s^{-1}. Utilizing the simultaneous measurements, a thermodynamically consistent elastic-plastic constitutive model including the von Mises yield criterion with the associated flow rule could be employed with a local heat diffusion equation to recreate the behavior exhibited during the test. The model was able to recreate the Lüders band phenomena and was also successful in capturing β_{diff}, which remains constant at 0.6 throughout the test.

The objective of the research detailed in this report is to determine the proportion of plastic work converted into heat during tension tests on Aluminium 2024 at strain rates ranging from quasi-static conditions up to 6000 s^{-1}. This entails determination of the Taylor-Quinney Coefficient for

Aluminum 2024 to increase the accuracy of the *MAT_224 material card for use in impact simulations.

1.2 Background on compression torsion testing of thin-walled tubes

Previously, thin-walled tube specimens were subjected to axial torsional loading to experimentally determine the dependence of equivalent fracture strain on the state of stress for 2024-T351 aluminum (Seidt, 2014). Axial torsional tests on thin-walled tube samples proved to be an efficient way to test samples under a wide range of plane-stress state conditions. By modifying the axial stress to shear stress ratio, stress triaxialities between -1/3 and p +1/3 and Lode parameters between -1 and +1 are theoretically achievable. Axial stress to shear stress ratio were controlled using load and torque control on an Instron 1321 biaxial load frame. The test series previously conducted included experiments under tensile torsion loading at two stress ratios (LR1: $\frac{\sigma_x}{\tau_{xy}}$ =~2.59, LR2: $\frac{\sigma_x}{\tau_{xy}}$ = ~1.15), pure torsion (LR3: $\frac{\sigma_x}{\tau_{xy}}$ = 0) and one compression-torsion stress ratio (LR4: $\frac{\sigma_x}{\tau_{xy}}$ = ~-0.92). This test series was conducted on two sample geometries: one for tension torsion loading and torsion only and one for compression torsion loading. The sample geometries were similar, however, compression-torsion specimen gages sections were shorter and thicker to reduce the likelihood of early buckling under compression. After the first test series was conducted, analyzed, and integrated into the material model it was determined that an additional compression torsion test was necessary. One additional axial torsional test series was conducted using $\frac{\sigma_x}{\tau_{xy}}$ = ~-1.70 (designated LR5). Results from this additional test series are presented in section 3 of this report.

1.3 Background of fracture testing under in-plane biaxial tension and out-of-plane compression

Accurate modeling of ductile fracture of metals on the continuum scale is of great importance. Finite element analysis is used in many engineering applications to design structural components and to simulate manufacturing processes. The material properties are entered into the calculations through material models. Since ductile fracture is preceded by a significant amount of plastic deformation, accurate prediction of ductile fracture depends on reliable material models for plasticity. On the microstructural scale, ductile fracture is a process that starts by the

nucleation of voids. As the deformation continues, damage accumulates in the form of void growth and coalescence, leading to final fracture. Ductile fracture has been modeled in various length scales. The interest in this report is in identifying a practical phenomenological approach where damage accumulation and final fracture are modeled in terms of stresses and strains on the continuum scale.

Following Rice and Tracey (1969), early ductile fracture models (Hancock & Mackenzie, 1976; Mackenzie, Hancock, & Brown, 1977) postulated that the accumulation of damage during plastic deformation depends on the triaxiality σ^* (the ratio between the hydrostatic component of the stress and the effective/von Mises stress), and that for a given state of stress, fracture occurs when the equivalent plastic strain reaches a critical value. A phenomenological fracture criterion is then determined from experimental data points that provide the value of the equivalent strain to fracture at different values of triaxiality. The data points are obtained from tests in which material coupon specimens are subjected to loads with different triaxialities. The value of the triaxiality and the corresponding equivalent plastic strain at the fracture location are determined from finite element simulations of the experiments. Typical tests that have been used for obtaining data points are uniaxial tension ($\sigma^* = 1/3$), tension of notched round specimens ($\sigma^* = 0.4 - 0.95$), pure shear ($\sigma^* = 0$), and uniaxial compression ($\sigma^* = -1/3$); (Børvik, Hopperstad, & Berstad, 2003; Hopperstad, Børvik, Langseth, Labibes, & Albertini, 2003; Seidt, 2010). In addition, several more complicated tests, like combined tension-shear and punch tests, have been developed for obtaining additional data points (Bao & Wierzbicki, 2004; Mohr & Henn, 2007).

Results from testing many metals show that consistent correlation between the equivalent strain to fracture and triaxiality exists for negative triaxialities (compression), and large positive triaxialities (tension). For negative triaxialities, materials are more ductile when damage is suppressed at large negative values, and the ductility monotonically decreases with smaller values of negative triaxiality. At sufficiently large positive values of triaxiality the hydrostatic component of the stress dominates damage accumulation by void growth and coalescence through material necking between the voids, and ductility decreases with increasing triaxiality. At small values of triaxiality, either negative or positive, the correlation between the strain to fracture and triaxiality is not consistent. The shear component of the stress affects void coalescence and using triaxiality alone to predict ductile fracture is not sufficient. For example,

for testing of 2024 aluminum, Seidt (2010) showed that the fracture strain in pure shear ($\sigma^* = 0$) is smaller than in uniaxial tension ($\sigma^* = 1/3$). This complex experimental data is impossible to model with a single relatively simple phenomenological mathematical expression that calculates the equivalent strain to fracture as a function of triaxiality only. One approach to modeling this complexity is to divide the triaxiality domain into three regions and use different mathematical expressions to model each region; (Bao, 2003; Bao & Wierzbicki, 2004).

Another approach is to attempt to account for the effect of shear on ductile fracture. This is done by the introduction of a new class of fracture criteria where, in addition to triaxiality, the equivalent strain to fracture is also a function of the Lode parameter, which is related to the third invariant of the deviatoric stress tensor; (Barsoum & Faleskog, 2007; Gao & Kim, 2006; Xue, 2007; Zhang, Bai, & Francois, 2001). In these models the fracture criterion is represented as a three-dimensional surface of the equivalent strain to fracture as a function of triaxiality and Lode parameter. The determination of experimental data points for creating such a fracture surface requires loading tests with various combinations of triaxiality and Lode parameter, which is not a trivial task.

Ideally, the tests should be designed to have proportional loading such that the triaxiality and Lode parameter remain constant throughout each test. In reality, however, these conditions almost never exist. Ductile fracture is preceded by a significant amount of plastic deformation that may change the specimen geometry during the test, which in turn affects the state of stress at the point that eventually fractures. Thus, proportional loading at the specimen boundary does not guarantee proportional increase of the stresses at the failure point and constant values of the triaxiality and Lode parameter throughout the test. Therefore weighted average values of the triaxiality and Lode parameter are calculated and used. In addition, direct measurement of the strain at the fracture point can also be challenging. The availability in recent years of the DIC technique for measuring deformation made it possible to measure the strain directly if the fracture occurs on the specimen's surface and the surface is visible to a camera.

Because of the above complexities inherent in testing ductile materials, the triaxiality, Lode parameter, and fracture strain are usually determined by a combined numerical-experimental approach. The testing configuration is simulated by assuming a plasticity model, and calculated quantities that can be measured in the experiment are compared. These quantities are the history

of the applied forces and/or moments, displacements and strains. If the simulations agree with the measurements, it is assumed that the calculated history of the stresses (i.e., the triaxiality and Lode parameter) and the equivalent strain at the failure point represent the material response.

Examples of fracture models that use the triaxiality and Lode parameter are the extended Mohr-Coulomb model (Bao & Wierzbicki, 2010; Labuz & Zang, 2012) and the Hosford-Coulomb model (Mohr & Marcadet, 2015). The Mohr-Coulomb failure criterion is dependent on the first and third principal stresses, and can be represented as a linear failure envelope tangent to Mohr's circle, where the tangent point between the failure envelope and Mohr's circle is the critical combination of normal and shear stress that will cause failure for a given mean stress (Labuz & Zang, 2012). In the extended Mohr-Coulomb model, the mathematical equations governing failure in terms of normal and shear stress are converted to being dependent on Lode parameter and triaxiality. Then, through use of a generalized hardening function to relate equivalent stress to equivalent strain, an equation relating equivalent failure strain to Lode and triaxiality can be found (Bao & Wierzbicki, 2010). The Hosford-Coulomb model is similar to the Mohr-Coulomb model, except that the Hosford equivalent stress is used so that this model is dependent on all three principal stresses, as opposed to the Mohr-Coulomb model that does not take into account the second principal stress. Similarly to what is done for the extended Mohr-Coulomb model, the Hosford-Coulomb model can likewise be expressed in terms of the equivalent failure strain, Lode parameter, and triaxiality (Mohr & Marcadet, 2015). This mathematical relation between the effective failure strain, Lode parameter, and triaxiality in the models is often represented as a 3-dimensional failure surface, and the shape and level of this surface can be tuned by parameters in the underlying mathematical equations (Bao & Wierzbicki, 2010).

Another approach, besides mathematically-based fracture models, are tabulated models. In tabulated models the material behavior is not represented by equations that were fitted to test data. Instead, the material response is determined using interpolation from tabulated data from tests at different conditions. One such tabulated model is MAT224, a plasticity and ductile fracture model in the finite element program LS-DYNA. It is a tabulated model that is based on the Johnson-Cook viscoplasticity, and fracture models (Johnson & Cook, 1983; Johnson & Cook, 1985). In the Johnson-Cook model plastic deformation is a function of strain, strain-rate, and temperature, and the fracture strain is a function of triaxiality. The plasticity part in MAT224

is similar to Johnson-Cook model but the fracture criterion is a three-dimensional surface of equivalent strain to fracture as a function of triaxiality and Lode parameter, similar to the extended Mohr-Coulomb and Hosford-Coulomb models. However, the surface in MAT224 is constructed from data points obtained from tests with different combinations of triaxiality and Lode parameter.

The MAT224 material model has recently been set up for 2024 aluminum and used in simulations of ballistic impact experiments (Park, Kelly, DuBois, Condasco, & Kan, 2020). The initial simulations did not predict the experiments well, and comparison of the simulations with the results of the impact experiments show that fracture takes place at points where the state of stress consists of biaxial in-plane tension and out-of-plane compression. This state of stress is in a region on the fracture surface that did not have data points from independent tests. The objective of the research presented here is to design and conduct a new independent test for determining the equivalent plastic fracture strain in a material subjected to a state of stress of in-plane biaxial tension and out-of-plane compression. Fracture under this state of stress is common in ballistic impacts.

2 Test Results on conversion of plastic work into heat over a wide range of strain rates in 2024-T351 Aluminum

2.1 Experiment techniques

2.1.1 Test specimens

Tensile tests are conducted on miniature dog-bone specimens (Figure 1) at strain rates of 1 E-4 s^{-1}, 1 E-1 s^{-1}, 1 s^{-1}, 500 s^{-1}, 2000 s^{-1}, and 6000 s^{-1}. The specimen geometry is consistent with that used previously to characterize 2024-T351 aluminum over a wide range of strain rates (Seidt, 2010).

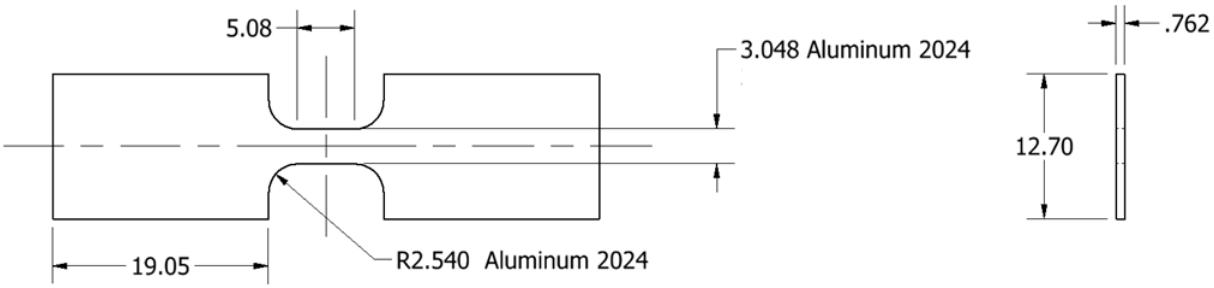

Figure 1. Miniature tension specimen geometry for 2024-T351 aluminum.

These miniature samples were used to ensure compatibility with the split-Hopkinson bar (SHB) apparatus used in this study. Modifications were made to the tabs of each specimen to allow for the specimen to be attached to each loading apparatus. The specimens for load frame had an increased tab length of 31.75 mm while those tested on the direct tension SHB had 3.97 mm diameter through holes in the center of the tab. These modifications did not affect the gage area of the specimen and should not affect the experimental results. To ensure consistency with previous results, each specimen was electric discharge machine (EDM) wire cut from 0.5” thick 2024-T351 aluminum plate and the re-cast layer from the EDM was ground off to reach a sample surface finish of 32 μin or lower. All samples were fabricated such that the gage loading direction was oriented in the rolling direction or the plate. An inconsistent surface finish can result in differences in emissivity and a reduction in the material strength properties between comparable specimens (Seidt, Pereira, & Gilat, 2015). The width and thickness of each specimen was measured before each test to ensure that slight variances in the machining and grinding of each individual specimen does not affect the calculation of engineering stress.

2.1.2 Experimental setup

An overview of the test program is shown in Table 1.

Table 1. Tensile test matrix to for plastic work to heat conversion study

Strain Rate (s^{-1})	Experimental Apparatus	Target Actuator Velocity
1.00E-04	Hydraulic Load Frame	5.08E-4 mm/s
0.1		0.508 mm/s
1		5.08 mm/s
500	Direct Tension Split-Hopkinson Bar	2.54 m/s
2000		10.16 m/s
6000	Direct Impact Split-Hopkinson Bar	40.64 m/s

Tests at strain rates ranging from 1E-4 s^{-1} to 1 s^{-1} were conducted on an Instron 1321 servohydraulic load frame apparatus. Tests at strain rates ranging from 500 to 2000 s^{-1} were conducted on a direct-tension SHB apparatus (Staab, 1991). Tests at 6000 s^{-1} were conducted on a striker-tube SHB apparatus. The load frame setup on Instron 1321 servohydraulic load frame is shown in Figure 2.

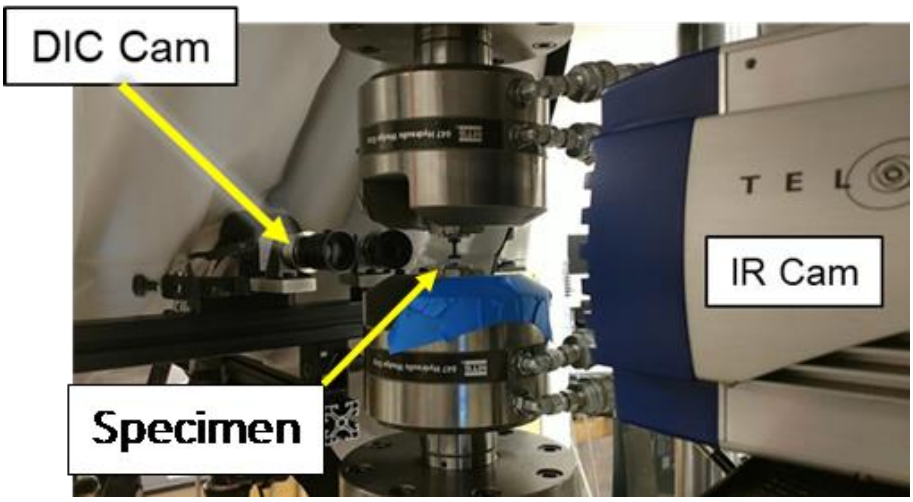

Figure 2. Low strain rate tension experimental setup on Instron 1321 servohydraulic load frame.

The sample is gripped using hydraulic wedge grips. One side of the sample is painted with a speckle pattern and is witnessed with a pair of Photron MC2 high speed cameras for DIC measurements, while the opposite side is unpainted and witnessed with the Telops FAST-IR camera. The MC2 cameras were used to determine the full-field displacement and strain fields directly on the surface of the specimen. The MC2 cameras have full resolution of 512x512 pixels and can run at frame rates up to 2000 fps (frames per second) without windowing. The FAST-IR camera has an InSb sensor, sensitive to the 3-5 µm spectral range and has full resolution of 320x256 pixels. The camera can operate at frame rates of 2000 fps at full resolution. For all three experimental setups, an LED light source from Visual Instrumentation Corporation is used to illuminate the side of the specimen witnessed by the visible cameras. This light source is well suited to these experiments, since LED lights have negligible IR signature and hence, negligible effect on the measurements from the IR camera. The Telops FAST-IR camera is used to measure temperature on the opposite side of the tension sample. Visible and IR camera settings (resolutions, frame rates, etc.) are presented in Table 2 and Table 3, respectively. MC2 full-resolution frame rates ranged from 0.2 fps to 2000 fps, depending on the strain rate. The Telops camera was run at full resolution (256 x 256) at framer rates identical to the visible cameras.

Table 2. Visible camera settings

Strain Rate (s^{-1})	Camera	Pixel Resolution	Frame Rate (fps)
1 E-4	2 x Photron MC2	512x512	0.2
0.1			200
1			2,000
500	Shimadzu HPV-X2	400x250	200,000
2000			625,000
6000			1,000,000

Table 3. IR camera (Telops Fast-IR) Settings

Strain Rate (s^{-1})	Pixel Resolution	Exposure Time (µs)	Frame Rate (fps)
1 E-4	256x256	50-100	0.2
0.1		20-50	200
1		10	2,000
500	64x20	10	20,000
2000	64x16	5	62,500
6000	64x4	5	90,000

The dynamic tension setup using the direct tension SHB apparatus is presented in Figure 3.

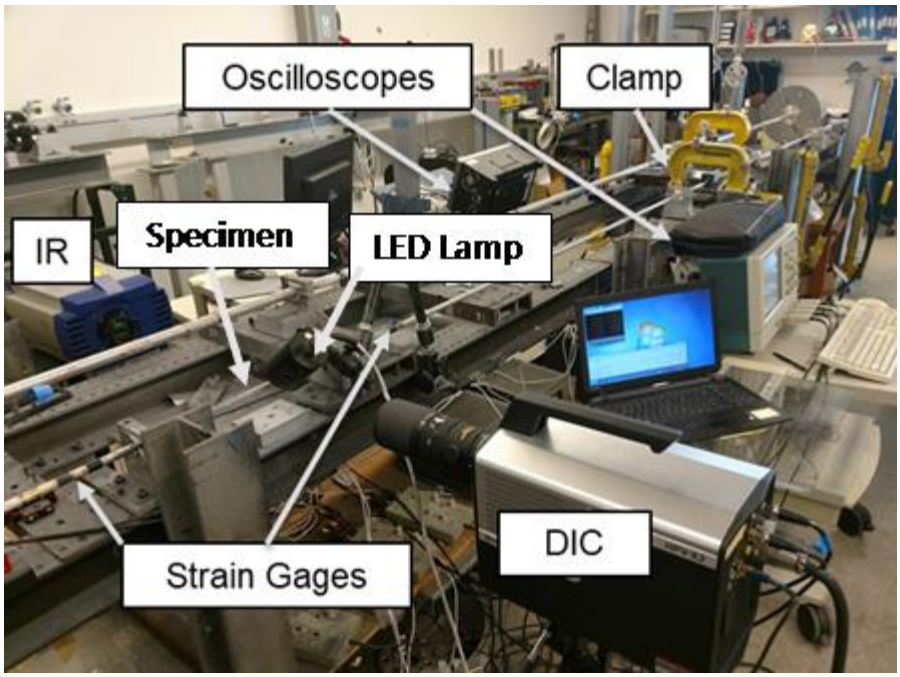

Figure 3. Dynamic tension experimental setup on direct tension SHB apparatus

This device is used to deform the 2024 tension samples at two nominal strain rates (500 s^{-1} and 2000 s^{-1}). The apparatus, schematically shown in Figure 4 uses a stored tensile load in a clamped section of the incident bar to generate the tensile loading wave (Staab, 1991).

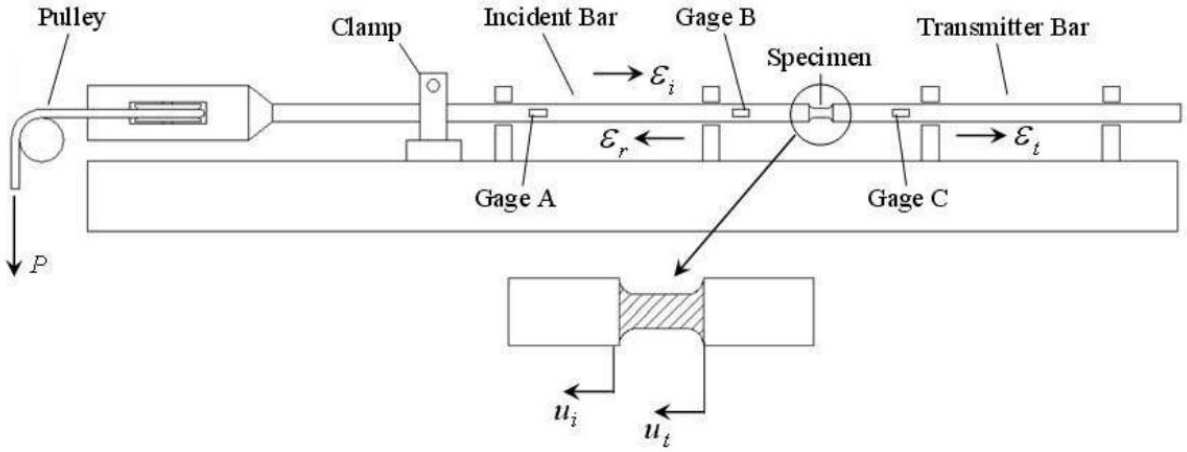

Figure 4. Direct tension (stored force) SHB apparatus

The stored tensile load is released by mechanically fracturing a consumable, aluminum pin. When this happens, the loading wave propagates to the specimen and applies dynamic tensile

loading to the sample. In this experiment, strain gage records used to calculate stress, strain rate and strain in the sample were measured by an oscilloscope. In addition, a Shimadzu HPV-X2 high speed camera is used to record the deformation of the specimen and to calculate full-field displacement and strain using 2D DIC. The Telops FAST-IR camera is used to measure temperature on the opposite side of the tension sample. HPV-X2 and Fast-IR camera settings for these tests remained as listed in Table 2 and Table 3.

A second oscilloscope was used to record trigger signals used to control each camera and the *actual sensor exposures* for both the HPV-X2 and FAST-IR cameras: a necessary measurement to synchronize and understand the DIC and IR temporal data since the frame rates are asymmetric.

The dynamic tension setup using the striker tube/transfer flange tension SHB apparatus is presented in Figure 5.

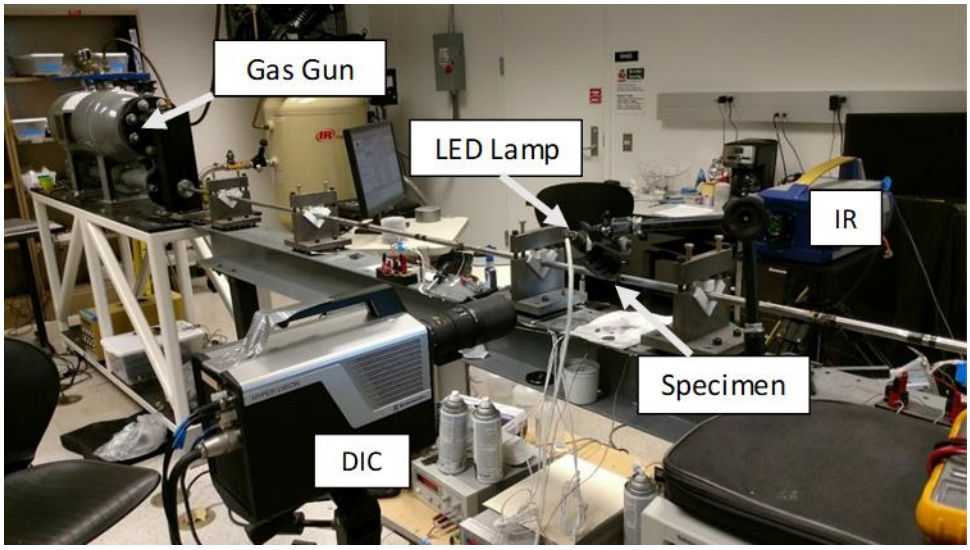

Figure 5. Dynamic tension experiment setup on striker tube tension SHB apparatus

This device is used to deform the 2024 tension samples at a nominal strain rate of 6000 s^{-1}. The apparatus, schematically shown in Figure 6, uses pneumatically fired striker tube that rides along the outside surface of the incident bar to generate the tensile loading wave.

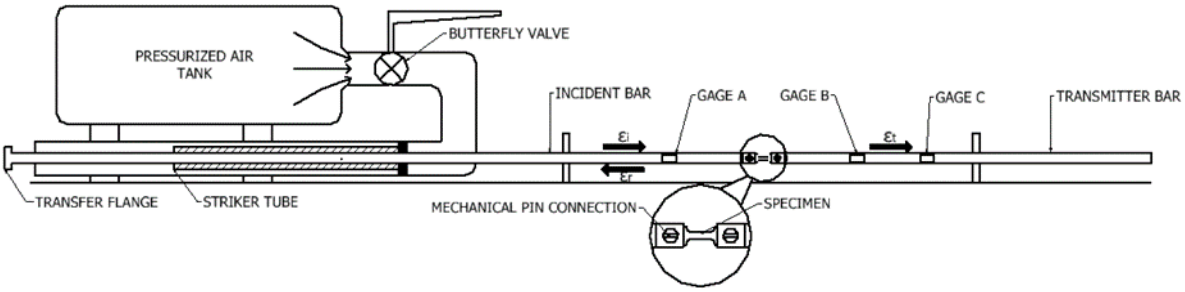

Figure 6. Striker tube/transfer flange SHB apparatus

When the tube strikes a transfer flange at the end of the incident bar, a tensile loading wave propagates to the specimen and applies dynamic tensile loading to the sample. Strain gage records and visible and IR images are recorded using an oscilloscope, the Shimadzu HPV-X2 and the Telops FAST-IR as discussed above. HPV-X2 and Fast-IR camera settings for these tests remained as listed in Table 2 and Table 3. A second oscilloscope recorded trigger signals and the *actual sensor exposures* for both the HPV-X2 and FAST-IR cameras due to frame rate asymmetry.

2.1.3 FAST-IR Temperature Calibration

The Telops FAST-IR camera records the flux of the photons emitted from the surface of each test specimen. Each individual pixel on the camera sensor has its own radiometric calibration, which allows for automatic compensation of ambient temperature drift and instrument self-radiance while implicitly controlling the exposure times and frame rate. The analog data collected by the camera sensor is digitized information in either photon counts, in-band radiance values $\left(\frac{W}{m^2-sr}\right)$, or radiometric temperatures (^{o}C). When making in-band radiance or radiometric calculations the control software HYP-IR assumes that the target of the camera is a black body and its emissivity is 1. However, the emissivity for Aluminum 2024 can be as low as 0.03, depending on the level of polish or oxidation on the sample surface (Del Campo, et al., 2010). Because of this discrepancy, a calibration must be conducted to determine accurate surface temperature measurements during each test.

Calibration was conducted by attaching thermocouples to 2024 tension specimens and resting the specimens on a hot-plate, shown in Figure 7.

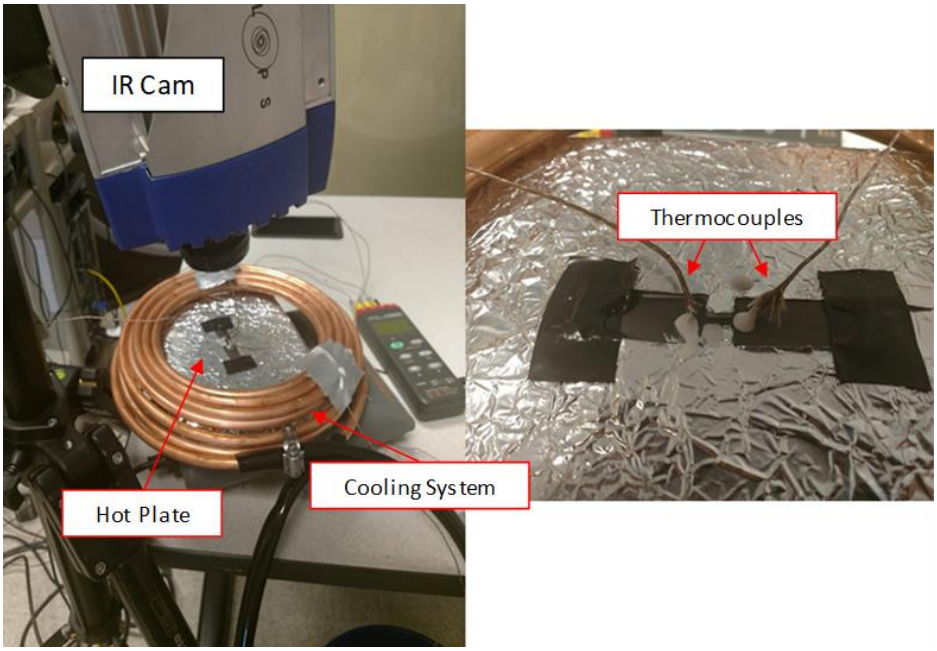

Figure 7. Hot plate calibration setup for FAST IR camera

The surface of the hot plate surrounding the specimen is covered in wrinkled aluminum foil that reduces noise by reflecting ~99.97% of incident radiation and emitting ~0.03% of the radiation due to an increase in temperature. A calibration run consists of heating the specimen to a temperature of ~80 °C or the camera saturation temperature, which depends on the camera settings inTable 3 (primarily exposure time) and then cooling the sample back to room temperature. The actual specimen temperature is measured using an Omega Type-K thermocouple attached to a temperature data-logger and the in-band radiance is measured by the IR camera. Cold water is run through a copper tube cooling coil to efficiently cool the hot plate and specimen back to room temperature to make the calibration process more efficient.

During the calibration, the IR camera records in-band radiance values for the entire visible gage section area. It is important to note that the calibration must be conducted at the same camera parameters as listed in Table 3. Therefore six separate calibrations must be conducted to cover the range of parameters listed in the table. The calibration results ***of all six calibrations*** are presented as the blue points in Figure 8, a plot of temperature measured by thermocouple vs in-band radiance data from the IR camera.

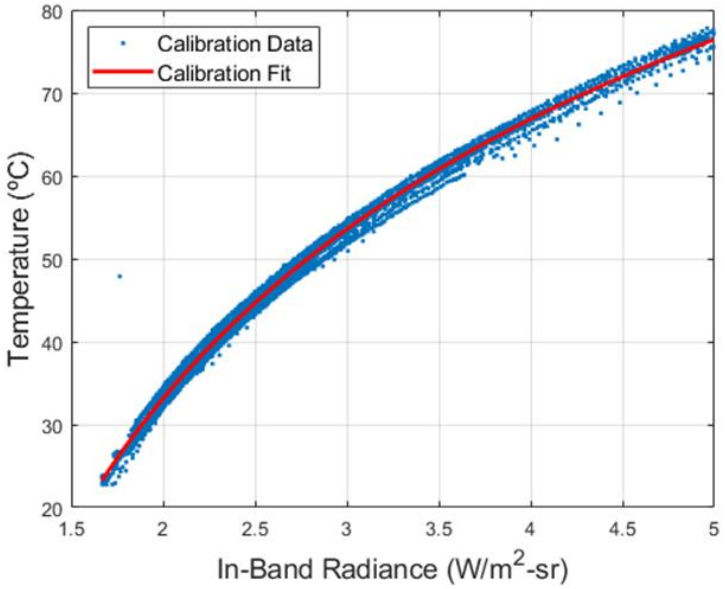

Figure 8. Temperature vs in-band radiance for 2024-T351 aluminum

The red curve in the figure is a best fit power-law according to Equation 3:

$$T = a * IBR^{b} + c \quad (3)$$

Where T is the temperature, IBR is the in-band radiance and a, b and c are fit coefficients. For aluminum 2024, the fit coefficients are; a =-246.5, b =-0.2572, c = 239.4.

These parameters, with equation 3 are used to convert in-band radiance values from the mechanical experiments to surface temperature in ℃.

2.2 Experiment results

Representative true stress vs. true strain curves from each of the strain rates conducted are presented in Figure 9.

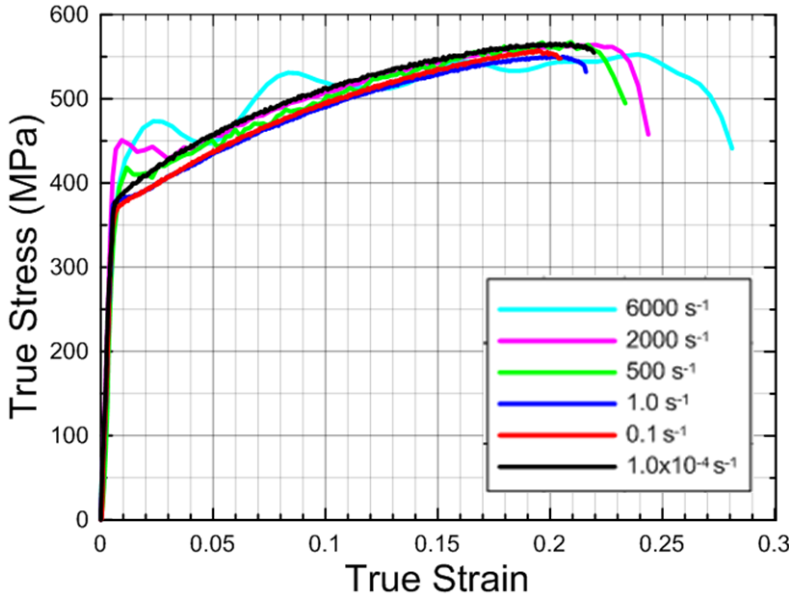

Figure 9. True stress vs. true strain for 2024-T351 tension tests at various strain rates

The curves show minimal strain rate sensitivity over the strain rate range tested (1E-4 s^{-1} to 6000 s^{-1}). This observation agrees with previously recorded data on dynamic tensile tests on the same 2024-T351 plate (Seidt, 2014). Figure 10 is a plot of measured temperature increase vs local Hencky strain ***at the localization (necking) and eventual failure point*** of the tensile sample.

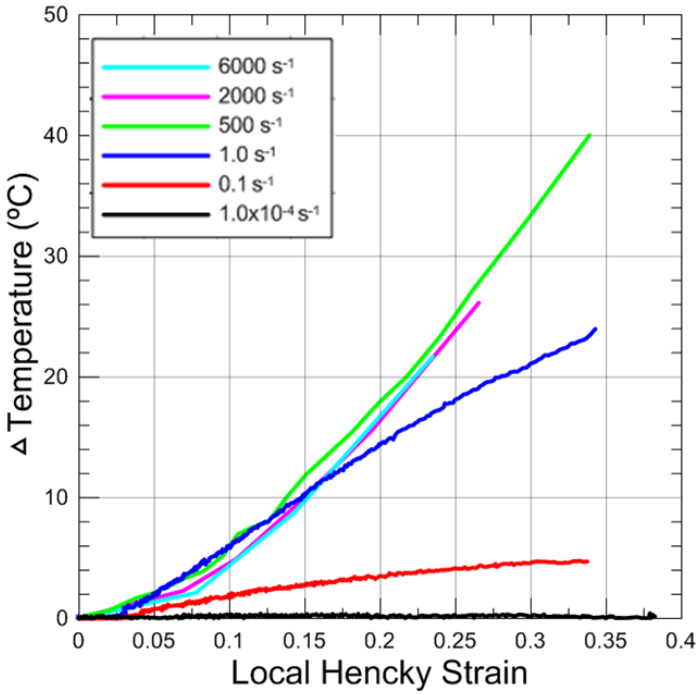

Figure 10. Change in temperature vs local tensile Hencky strain at specimen failure point for 2024-T351 aluminum

Like Figure 9, Figure 10 includes a representative curve from each strain rate conducted, illustrating the transition from isothermal loading conditions at 1E-4 s^{-1} to adiabatic dynamic deformation at strain rates at and above 500 s^{-1}. It is interesting to note that modest temperature increase (about 5 °C) is observed at strain rates as low as 0.1 s^{-1}. At a strain rate of 1 s^{-1}, the material deformation is nearly adiabatic, reaching temperatures of ~25 °C immediately prior to specimen fracture. At strain rates at and above 500 s^{-1}, an identical trajectory of temperature vs strain is observed; evidence that adiabatic deformation is attained at a strain rate of at least 500 s^{-1}.

Time history data of representative tests from each of the strain rates are presented in Figure 11(a), (b), (c), (d), (e), and (f) represent tests at strain rates of 1E-4 s^{-1}, 0.1 s^{-1}, 1.0 s^{-1} 500 s^{-1}, 2000 s^{-1} and 6000 s^{-1}, respectively.

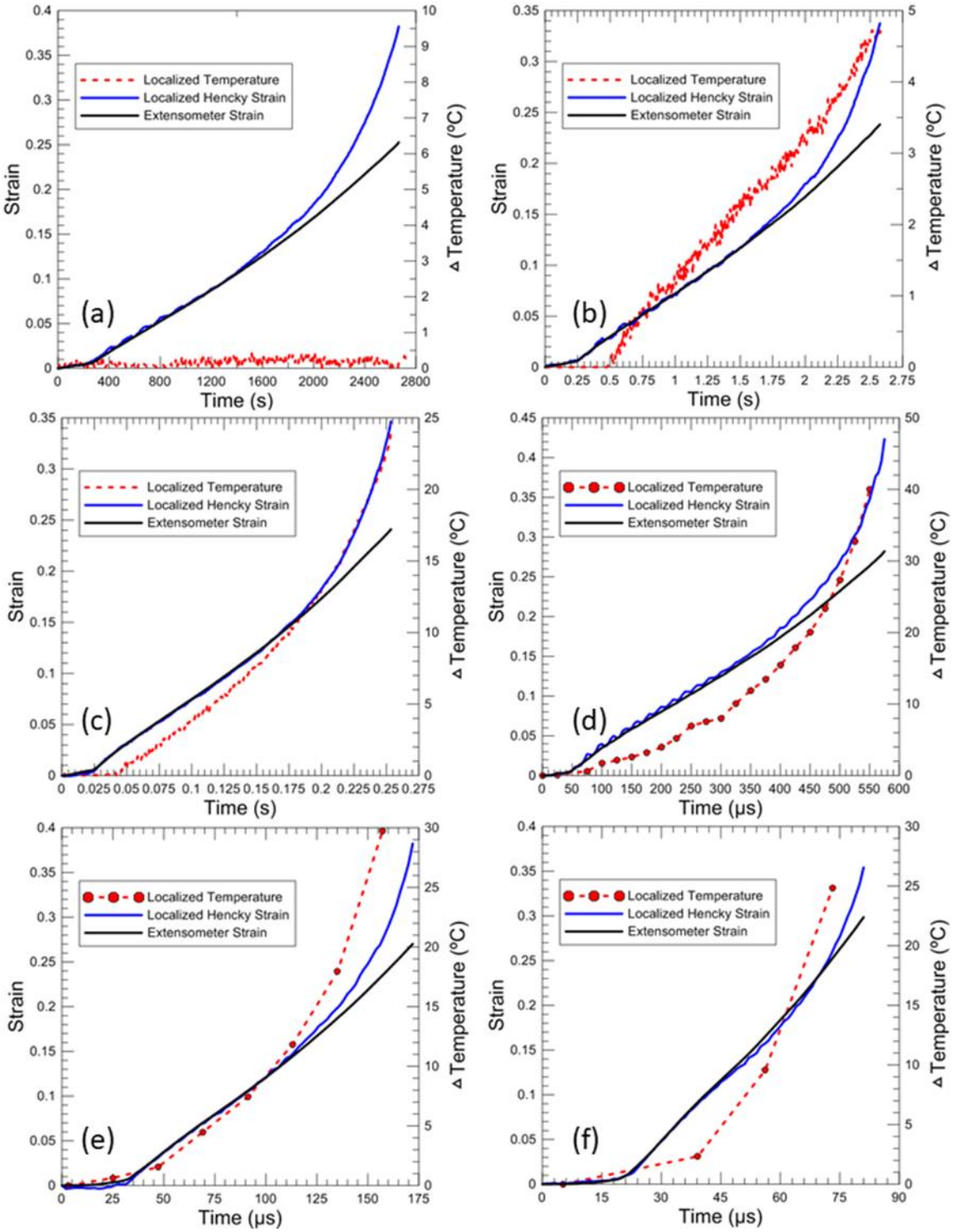

Figure 11. Strain and Temperature History for the Failure Point during Tension Tests of Aluminum 2024-T351 at Strain Rates of (a) 1E-4 s^{-1} (b) 0.1 s^{-1} (c) 1 s^{-1} (d) 500 s^{-1} (e) 2000 s^{-1} (f) 6000 s^{-1}

Two DIC strain measurements are plotted: engineering strain from a 4mm initially long extensometer (black curves) and the Hencky strain at the localization and eventual fracture location (blue curves). The red dashed curves show the temperature rise also in the localization/fracture region. The test durations range from ~2800 seconds, Figure 11(a): 1E-4 s^{-1} to about 90 μseconds in Figure 11(f): 6000 s^{-1}. The SHB test data in Figure 11(d)-(f), show each data point captured by the IR camera. The time resolution for the temperature measurement is acceptable for the tests at 500 s^{-1}, however at strain rates of 2000 s^{-1} andf 6000 s^{-1}, the time resolution from the IR camera is coarse, yielding only seven and four data points during the deformation, respectively. This is the reason that measured temperature rise is highest (40 °C) for the 500 s^{-1} tests and not the 2000 s^{-1} and 6000 s^{-1} tests.

Full-field strain, temperature, and Taylor-Quinney Coefficient data are presented in Figure 12 for a test at a nominal strain rate of 500 s^{-1}.

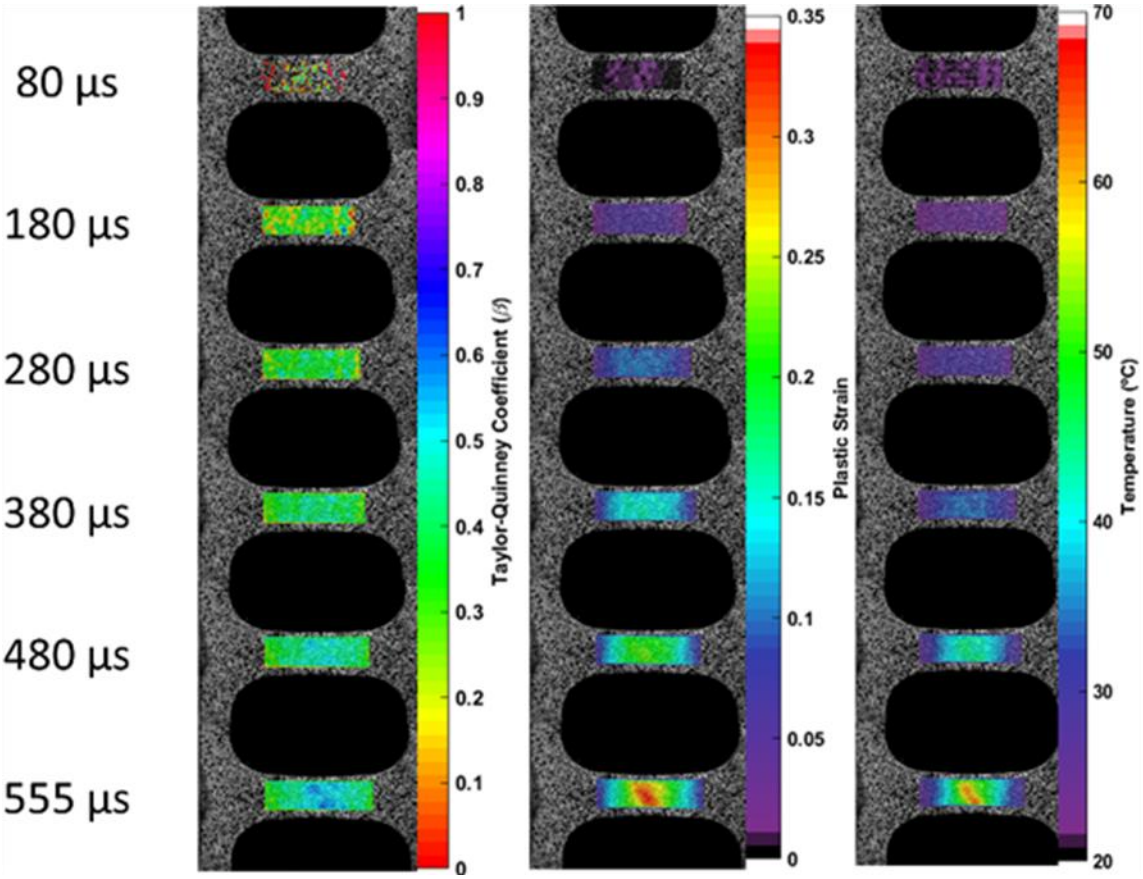

Figure 12. Full-field Taylor-Quinney, plastic strain and temperature measurements for an Aluminum 2024-T351 tension test at 500 s^{-1}

These plots were made by spatially synchronizing the DIC full-field strain data with IR temperature data. This is a non-trivial task, since the resolution (see Table 2 and Table 3) and field of view of the visible and IR cameras are not the same. Additional complexity arises from the fact that the DIC strain and IR temperature data are extracted from their respective software with different frames of reference. The DIC software tracks the subset positions with respect to the initial, undeformed image, describing a Lagrangian reference frame. The temperature data is reported at a fixed pixel location in the camera and does not measure the same point on the specimen for the duration of the test due to motion associated with deformation. A single point on the surface of the specimen will pass through multiple sensor pixels during deformation, describing an Eulerian frame of reference. To first synchronize the cameras spatially, images of a 9x9 grid of known spacing (A Correlated Solutions 3D calibration grid with 1 mm pitch) with both cameras are recorded. This allows a custom-coded MATLAB script to superpose the strain and temperature data fields. In every case, the visible (or DIC) cameras have higher resolution than the IR camera (see Table 2 and Table 3). The temperature at each DIC strain measurement point (or subset) is determined using 2D spatial interpolation from synchronized (temporal and spatial) DIC and IR images using MATLAB. More detail regarding the temporal and spatial synchronization of the DIC and IR data fields and the interpolation process are presented by Smith (2019).

With temporally and spatially synchronized strain and temperature data fields, the full-field Taylor Quinney Coefficient (Figure 12) can be determined from Equation 1. The denominator of Equation 1 is the integrated plastic work, which can be broken down into the integral of the stress multiplied by the strain as follows:

$$\beta_{int}(t) = \frac{\rho c_p (T(t) - T_0)}{\int_0^t \sigma_t(t)\epsilon_p(t)} \tag{4}$$

In Equation 4, the quantities are known: $T(t)$ and $\epsilon_p(t)$, are known from the spatially synchronized IR and DIC data fields, respectively and ρ and c_p (density and ratio of specific heat at constant pressure) are known from available handbook data for 2024-T351 aluminum. The final, unknown element in Equation 4 is the true stress in the material. True stress data, in an average sense, is known from the experimental records. The average engineering stress in the specimen is the load divided by the initial cross-sectional area. The true stress in Figure 9, for example, was

calculated using engineering stress (σ_E) and the engineering strain (ϵ_E) from a 4 mm initially long extensometer using the well known formula: $\sigma_t = \sigma_E(1 + \epsilon_E)$. This true stress value, however, is inconsistent with the full-field strain and temperature data we described above, since it is an average of the true strain of the sample along the entire length of the 4 mm extensometer. The virtual strain gage size from the DIC data and the virtual thermocouple sizes from the IR measurements are much smaller than 4mm, therefore, steps must be taken to determine full-field stresses that are consistent with the synchronized strain and temperature data. This is accomplished by using the Hencky strain tensor data from DIC. The Hencky strain tensor is a logarithmic definition of strain, essentially a continuum, tensorial definition of the true strain (Seidt, 2014). True stress can be determined from the simple equation σ_t=σ_E (1+ϵ_E), a function of engineering stress (a known quantity: load divided by initial cross-sectional area) and engineering strain (determined previously from a 4mm extensometer). The approach here is to determine a tensorial engineering strain on the same size scale as the DIC Hencky strain. This is done by using the equation: ϵ_t=ln(1+ϵ_E). Inserting equivalent Hencky strain values into ϵ_t in this equation, the tensorial engineering strain can be determined from: ϵ_E=exp(ϵ_t)-1. This, along with the known engineering stress can be used to calculate full-field true stresses using the definition of true stress presented above. This stress along with the Hencky strains from DIC and the Temperatures from the IR images can be inserted into Equation 3 to determine full field βint, shown in Figure 12. For these calculations, the following density and specific heat values were used:

$$\rho = 2780 \text{ kg/m3}$$

$$Cp = 875 \text{ J/kg-K}$$

The average Taylor-Quinney coefficient versus local plastic strain for all data points located within the localization (necking) region of each test is shown in Figure 13.

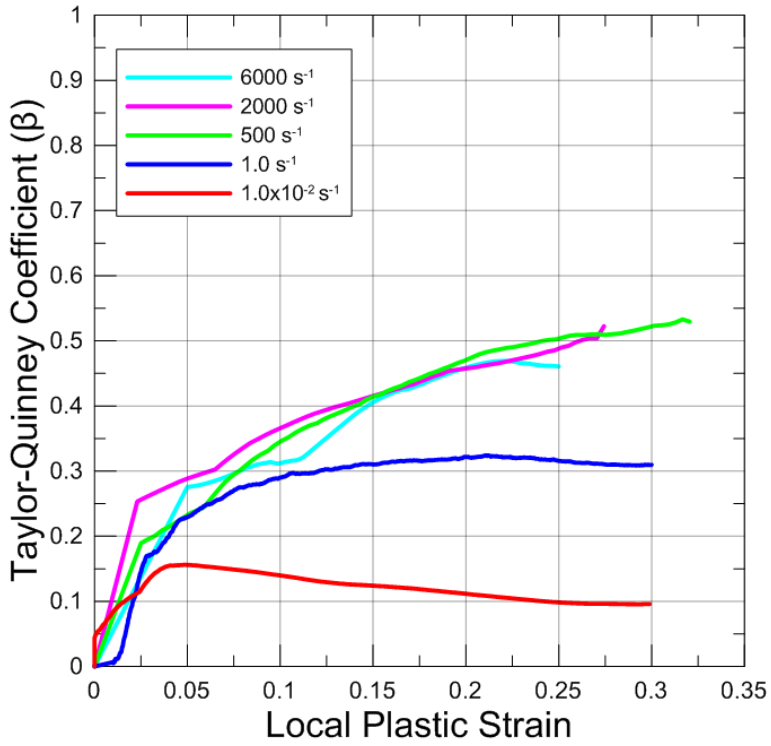

Figure 13. Taylor-Quinney coefficient versus local axial plastic strain in the localization (necking) region at various strain rates

A representative curve from each strain rate group is presented in the figure. At a strain rate of 0.1 s^{-1}, β increases from 0 to 0.15 as the strain increases from 0-0.05. Then, β steadily decreases to 0.1 at a plastic strain of 0.3. In the 1 s^{-1} test, β increases from 0 to 0.3 as the plastic strain increases from 0 to 0.1 and remains constant at 0.3 up to a plastic strain of 0.3. The trend for the tests from 500 to 6000 s^{-1} is nearly identical. The β increases from 0 to 0.3 as the plastic strain increases from 0 to 0.05 then steadily increases from 0.3 to 0.5 as the plastic strain increases from 0.1 to 0.3.

Average thermal energy densities within the sample localization regions ($\rho c_p \Delta T$) are plotted against the strain energy densities ($\int \sigma_t \, d\epsilon$) for each strain rate in Figure 14.

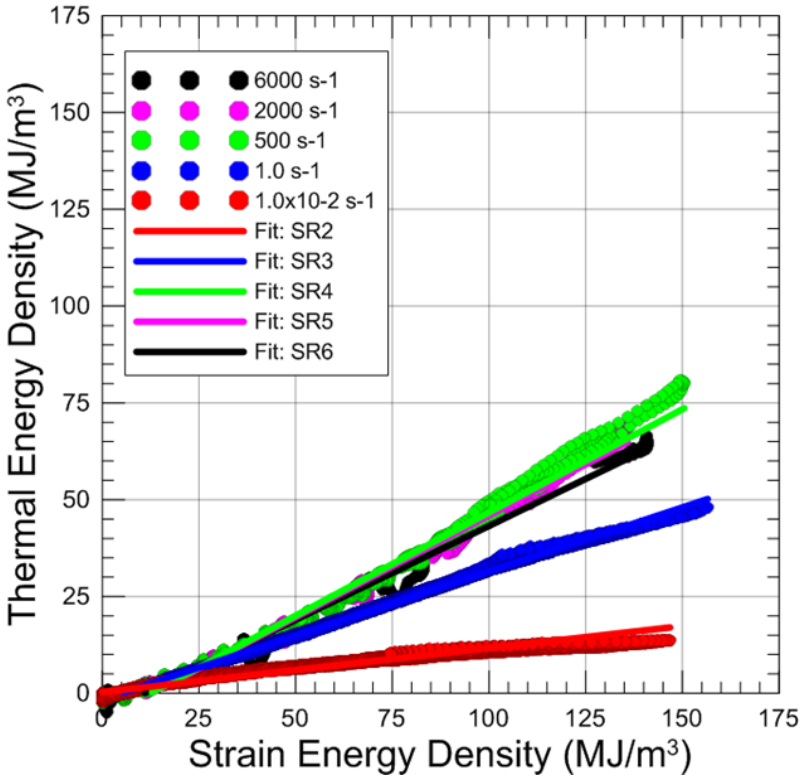

Figure 14. Thermal energy density vs strain energy density to calculate average β values for Aluminum 2024-T351

The average Taylor-Quinney Coefficient (β_{int}) can be determined at each strain rate by determining the linear slope to each data set. These values are summarized in Table 4.

Table 4. Average Taylor-Quinney coefficients (β) for aluminum 2024-T351 from energy density plots at various strain rates

Strain Rate (s^{-1})	**Average β from Slope**
0.1	0.114
1	0.331
500	0.533
2000	0.526
6000	0.485

The average β_{int} increases from 0.114 at a strain rate of 0.1 s^{-1} to ~.5 at strain rates greater than and equal to 500 s^{-1}. The average β_{int} magnitude peaks (0.533) at a strain rate of 500 s^{-1} and decreases to 0.526 and 0.485 at strain rates of 2000 s-1 and 6000 s-1, respectively. β_{int} is determined from a linear regression fit to the available data. At strain rates of 2000 s-1 and 6000 s-1, the IR camera frame rate limits the test data density. It is likely that the reduction in β_{int} is an erroneous artifact of this issue. It is recommended that β_{int} = 0.533 should be used for model development at all strain rates at and above 500 s^{-1}.

3 Compression torsion testing of thin-walled tube specimens

Compression torsion thin-walled tube samples are presented in Figure 15.

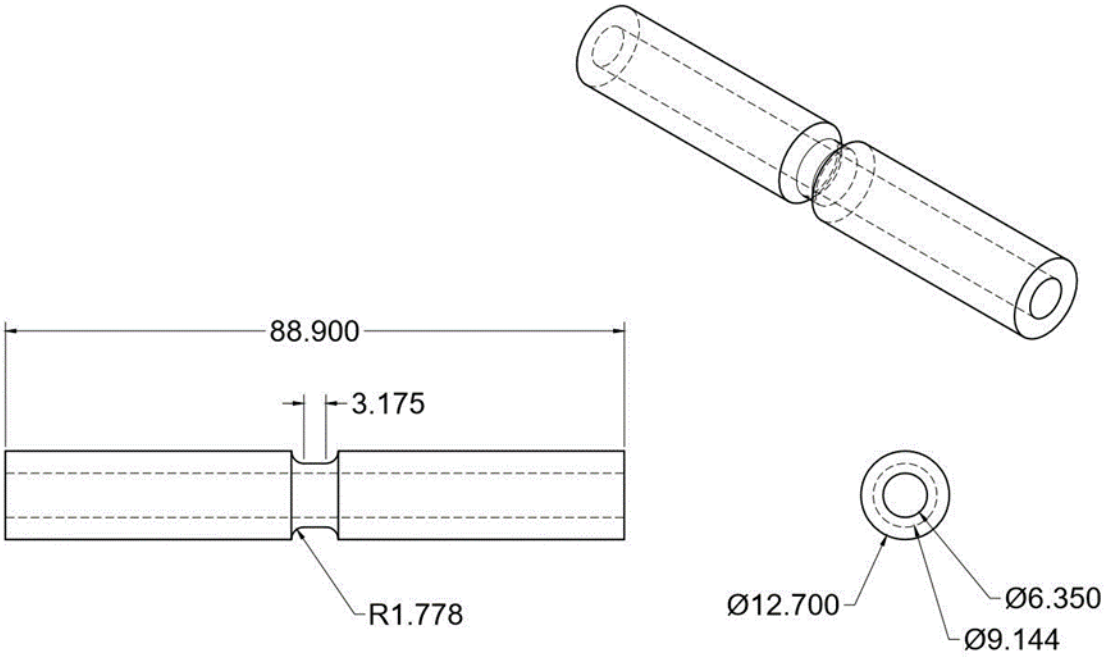

Figure 15. Compression torsion thin walled tube sample geometry (dimensions in mm)

The gage section of the sample is 3.175 mm (0.125 in) long and has 1.397 mm (0.055 in) thickness. The mean gage radius of the sample is 3.874 mm (0.153 in). The 12.7 mm diameter ends of the specimen are held, respectively in hydraulic wedge grips outfitted with V shaped wedges designed to hold a range of round sample diameters. The specimens were tested using an Instron 1321 hydraulic load frame capable of applying both axial (tensile/compressive) and torsional loading. Tests were conducted by setting the axial control channel to load control and the torsional control channel to torque control. Using the sample dimensions and the target axial to shear stress ratio ($\frac{\sigma_x}{\tau_{xy}}$ = ~-1.70), the ratio of the axial force to torque was determined. Linear ramps in axial load and torque were specified in the MTS 793 control software such that this axial load to torque ratio and hence the axial stress to shear stress ratio ($\frac{\sigma_x}{\tau_{xy}}$) was maintained through the entire duration of the test.

Test data from the LR5 combined compression-torsion test series are presented in graphic form below. Figure 16 shows the force vs displacement curves from all three tests conducted in the test series.

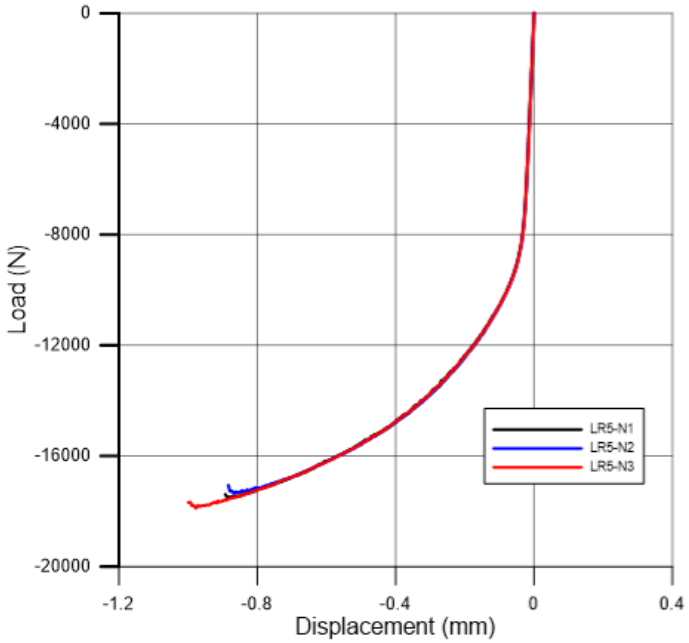

Figure 16. LR5 combined compression-torsion test series, force vs. displacement curves

Figure 17 shows torque vs rotation plots for the three tests:

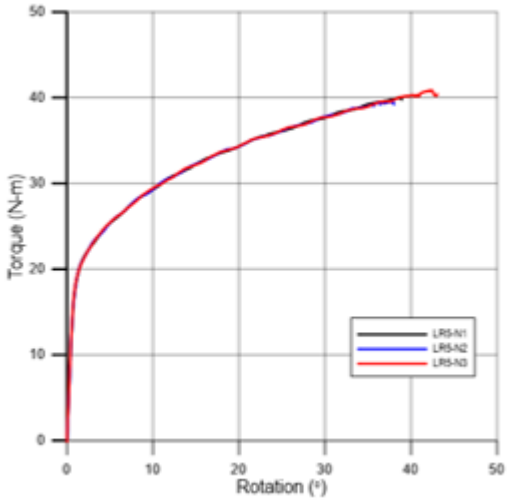

Figure 17. LR5 combined compression-torsion test series, torque vs rotation curves

Axial load and torque were measured using the integrated axial-torsional load cell on the Instron 1321 load frame. Displacement and rotation were determined using 3D DIC by calculating the relative displacement and rotation between two DIC extraction points located on the upper and lower grip shoulders of the tube specimen. The axial load and displacements are negative (sign convention showing compressive loads and deformation). The curves in Figure 16 and Figure 17 are quite repeatable. Figure 18 presents the Hencky strain histories (vs time) for each test.

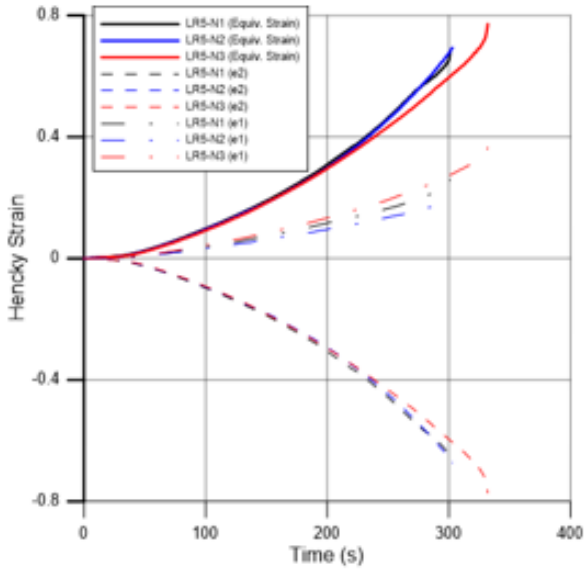

Figure 18. LR5 combined compression torsion test series, strain state at fracture location

Maximum principal strain curves for each test are identified by dashed curves while minimum principal strains are identified by dash-dot curves. Equivalent strain (solid lines) is computed using these two principal strain components and the assumption that the material conserves volume during plastic deformation (isochoric). If volume is conserved, the sum of the three Hencky principal strain components must equal zero. From that relationship the third principal strain (ε_3), and hence the equivalent strain ($\bar{\varepsilon}$) can be calculated according to Equations 5 and 6:

$$\varepsilon_3 = -(\varepsilon_1 + \varepsilon_2) \tag{5}$$

$$\bar{\varepsilon} = \sqrt{\frac{2}{3}(\varepsilon_1^2 + \varepsilon_2^2 + \varepsilon_3^2)} \tag{6}$$

For these tests, the major contributor to the equivalent strain is the minimum principal strain ε_2 (dashed lines). The magnitude of the equivalent strain is only slightly larger than the absolute value of ε_2. This test series illustrates the importance of determining the fracture strain dependence on stress state for ductile metals. These three tests have average equivalent strain at fracture of 0.715, substantially larger than the nearest stress state tested in this project (0.57 for combined compression torsion, LR4) and more than twice that at uniaxial tension (~0.30 for SG1 and SG5). Figure 19 presents the maximum and minimum principal strain fields from DIC measurements for a typical LR5 test on the left and right, respectively. Equivalent strain at fracture for the three experiments are summarized in Table 5.

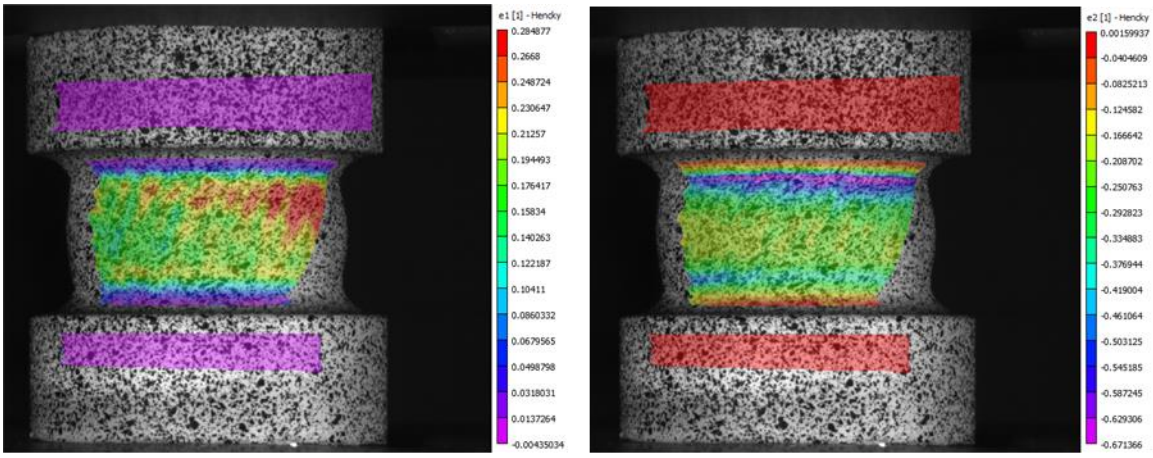

Figure 19. 3D DIC strain fields for test # M1-TMCL-LR5-P4-SR6-T1-N2: maximum principal strain (left), minimum principal strain (right)

Table 5. Fracture strain data summary of compression torsion LR5 test series.

Test #	Equivalent Strain at Fracture	Strain at Fracture	Standard Deviation
M1-TMCL-LR5-P3-SR3-T1-N1	0.6774	0.7142	0.04138
M1-TMCL-LR5-P3-SR3-T1-N2	0.6932		
M1-TMCL-LR5-P3-SR3-T1-N3	0.7720		

4 Fracture strain of 2024-T351 Aluminum under in-plane biaxial tension and out-of-plane compression

4.1 Experiment design

The objective was to design a test to determine the strain to fracture of a material element that is proportionally loaded to fracture under a stress state of combined in-plane biaxial tension and out-of-plane compression. A state of stress of equi-biaxial tension and out-of-plane compression can be written as Equation 7:

$$\sigma_{ij} = \begin{vmatrix} 1 & 0 & 0 \\ 0 & 1 & 0 \\ 0 & 0 & b \end{vmatrix} \sigma_{xx} \tag{7}$$

with $\sigma_{xx} > 0$ and $b = \sigma_{zz}/\sigma_{xx} < 0$. For a given state of stress σ_{ij} the triaxiality σ^* is defined by Equation 8:

$$\sigma^* = -\frac{\sigma_h}{\bar{\sigma}} \tag{8}$$

where $\sigma_h = \sigma_{kk}/3$ is the hydrostatic part of the stress and $\bar{\sigma} = \left(3/2\, s_{ij}s_{ij}\right)^{1/2}$ is the effective (von Mises) stress where $s_{ij} = \sigma_{ij} - \sigma_h\delta_{ij}$ is the deviatoric stress. The minus sign in equation (15) follows the definition of triaxiality in LS-DYNA (positive triaxiality in compression). The Lode parameter *L* is defined by Equation 9:

$$L = \frac{27}{2}\frac{J_3}{\bar{\sigma}^3} \tag{9}$$

where $J_3 = S_1S_2S_3$ is the third invariant of the deviatoric stress tensor, and S_1, S_2 and S_3 are the principal deviatoric stresses. Substituting the state of stress from Equation 7 in Equation 9 gives $L = -1$ for all values of *b*. The value of the triaxiality σ^* depends on the value of *b*. In a state of equi-biaxial tension $b = 0$ and $\sigma^* = -2/3$. When out-of-plane compression is added (*b* has a negative value) the triaxiality increases (becomes less negative). The triaxiality is zero when $b = -2$ (the magnitude of the out-of-plane compression is twice the magnitude of the in-plane biaxial tension), and becomes positive for more negative values of *b* (for example: $\sigma^* = 1/6$ for $b = -5$).

The experimental setup devised for subjecting material to a stress state of in-plane biaxial tension and out-of-plane compression through a small diameter punch test is shown schematically in Figure 20.

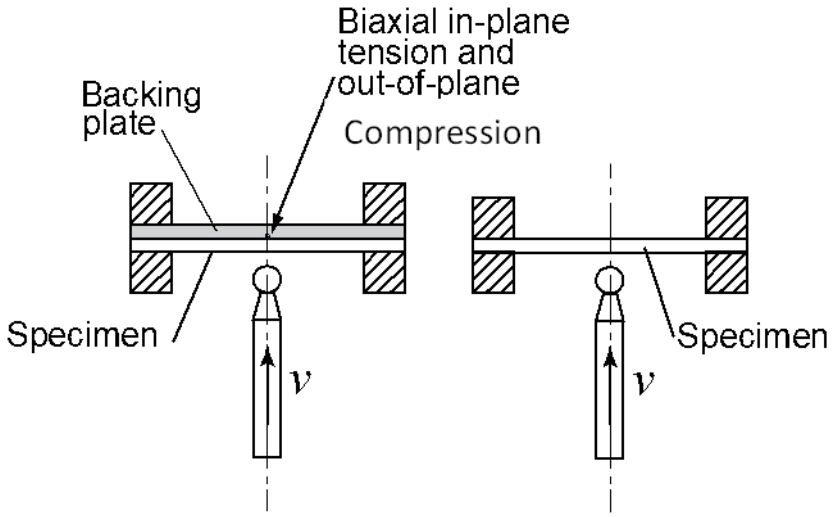

Figure 20. Punch test with a backing plate (left), and without a backing plate (right)

The object consists of a thin circular plate specimen made of the material to be tested that is backed by another plate of a different material. The plates are clamped to a fixed support around the circumference, and a small diameter punch is pushed into the specimen plate at its center. Upon loading, a stress state of biaxial tension and out-of-plane compression develops at the point of the specimen that is in contact with the backing plate along the center line of the punch. The magnitude of the out-of-plane compression stress (and thus the triaxiality) depends on the properties and the thickness of the backing plate. The backing plate needs to have sufficient stiffness, lower yield stress, and higher ductility than the specimen. A thicker backing plate results in higher compressive stress.

Tests were conducted with specimens made of 2024-T351 aluminum and backing plates made of annealed 110 copper. The testing plan included tests with backing plates of two different thicknesses, denoted thin-backed and thick-backed, and tests with unbacked specimen plates. The dimensions of the components used in the tests are listed in Table 6.

Table 6. Dimensions for punch tests with 2024 aluminum specimens and copper backing plate.

Case	Specimen Thickness (mm)	Backing Plate Thickness (mm)	Punch Diam. (mm)	Die Diam. (mm)
Unbacked	1.27	N/A	2.3	50.8
Thin-backed	0.635	1.27	2.3	25.4
Thick-backed	0.635	2.54	1.6	25.4

4.2 Experiment Setup

A photograph of the experiment setup is shown in Figure 21. The photo shows an aluminum specimen and a copper backing plate clamped together to a holding frame that is connected to the top of a hydraulic load frame.

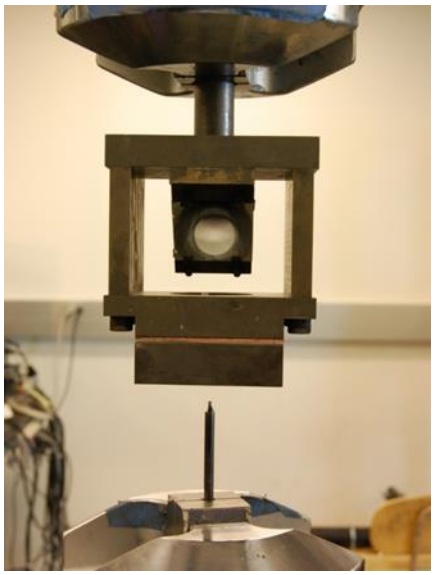

Figure 21. Experiment setup of a small diameter punch test of a specimen with backing plate

A small diameter punch was attached on the opposite side to the actuator of the machine. During a test the punch was displaced into the specimen. The force applied by the punch was measured by the load cell at the top of the frame, and the punch displacement is given by the stroke of the actuator. The back surface of the specimen (or the backing plate) was viewed through a 45° inclined mirror that is fastened to the fixture frame.

In unbacked tests the punch was pushed continuously into the specimen plate until it fractures. The force and displacement of the punch were recorded and the deformation of the back surface of the specimen was measured with DIC. A speckle pattern was applied to the back surface of

the specimen using black and white spray paint, and images were recorded during the loading period for DIC analysis.

Two different types of tests were performed when a backing plate was used, continuous and sequential. In continuous tests, the punch was pushed continuously into the specimen until fracture was detected. The punch force and the stroke were measured and fracture was detected when a reduction in the force was observed. The deformation of the back surface of the specimen was not measured during the continuous tests since the backing plate blocks the view. The deformation of the back surface of the specimen plate was measured in the sequential tests. Before conducting a sequential test, the back surface of the specimen (the surface that will be in contact with the backing plate) was painted with a speckle pattern and a clear Teflon lubricant coating is applied to enhance pattern survivability. The sequential test was conducted by loading the specimen in increments and, as illustrated in Figure 22, at each loading increment the test was interrupted, the specimen unloaded, removed from the loading fixture, placed in a holding fixture, and an image of the deformed speckle pattern on the back surface was taken for DIC analysis.

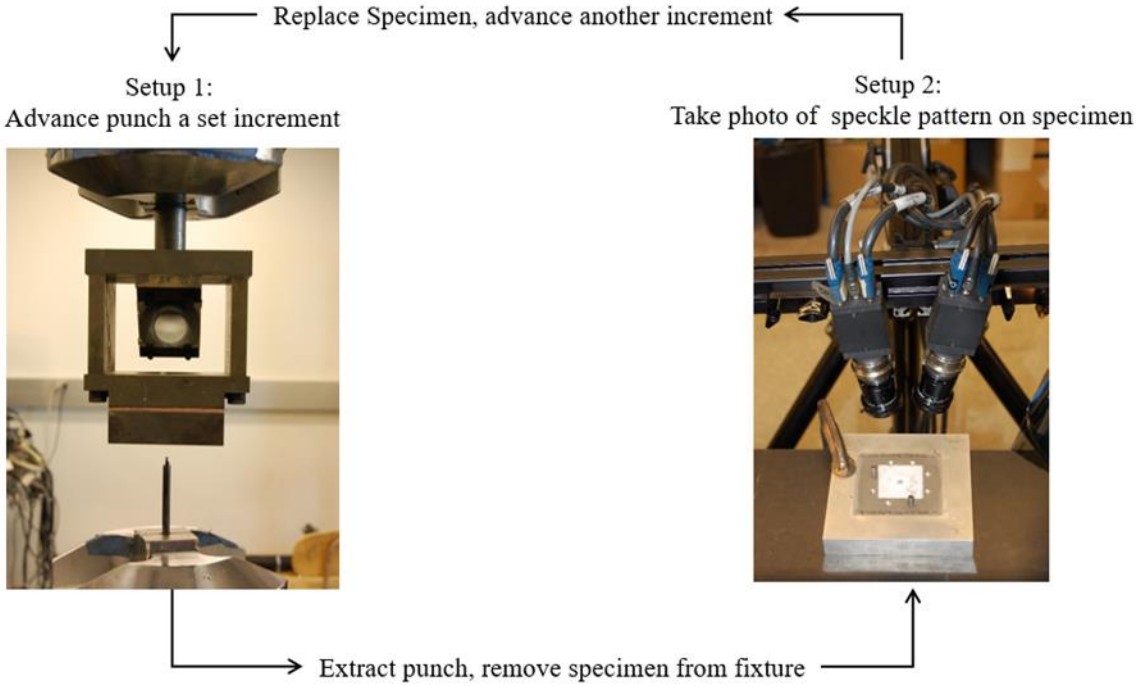

Figure 22. Illustration showing sequentially loaded punch test

The specimen and backing plate were placed back in the loading fixtures and another loading increment was applied. This process continued until fracture of the specimen was observed. To minimize friction, lubrication was applied between the back surface of the specimen and the backing plate and to the surface of the punch.

4.3 Experiment Results

The quantities measured in the experiments were the punch force, the punch displacement, and the strains on the back surface of the specimen. In addition, the location of the point where fracture was first observed and the instant when it occurred was identified. The history of the measured quantities was compared with the calculated values up to the point when fracture was first detected. If the calculations agree with the measurements, it was assumed that the calculated stresses and strains in the element at the fracture location were genuine and could be used for calculating the history and final values of the triaxiality, Lode parameter, and the equivalent plastic strain.

Results from the unbacked tests are displayed in Figure 23 and Figure 24. Figure 23 shows the measured punch force as a function of its displacement from three tests.

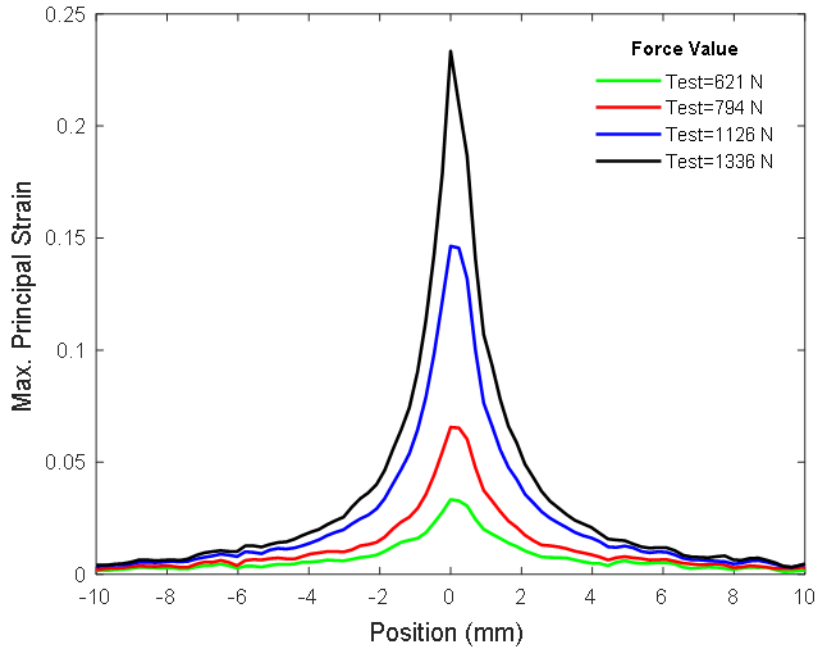

Figure 23. Maximum principal strain along the diameter line on the back surface of the specimen in an unbacked test at different punch force values

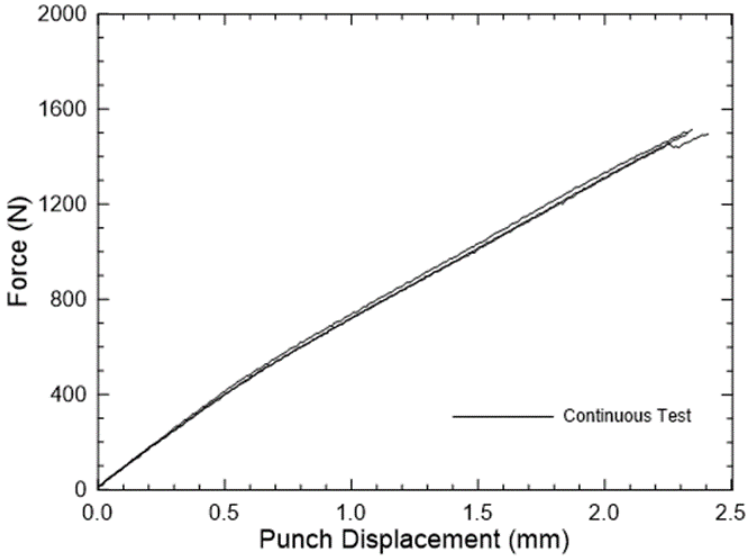

Figure 24. Punch force as a function of punch displacement in unbacked experiments

The curves are consistent with small scatter. In these tests, fracture is observed at an average punch displacement of 2.14 mm and average punch force of 1,400 N. The history of the

maximum principal strain at the back surface of the specimen from one of the unbacked tests is shown in Figure 24.

This figure shows “waterfall” plots of measured and calculated maximum principal strain along the diameter line on the back surface of the specimen at four values of punch force. The last curve (punch force of about 1,335 N) is just before specimen fracture. The history of the stress triaxiality, Lode parameter, and effective plastic strain in the specimen must be determined through parallel numerical simulations. This is done under separate cover (Park, Kelly, DuBois, Condasco, & Kan, 2020). For this specific and simple case (unbacked), we know that the stress triaxiality in the failed element will be very close to biaxial tension (a value of -2/3) and maintain a Lode parameter of -1.

Results from thin-backed plate tests are displayed in Figure 25 and Figure 26. Figure 25 shows measured punch force versus punch displacement curves from three tests where the specimen is loaded continuously up to fracture, and one representative curve from a sequential test where the specimen is loaded in thirteen steps until fracture occurs. Fracture is observed at an average punch displacement of 2.45 mm and average force of about 1,460 N.

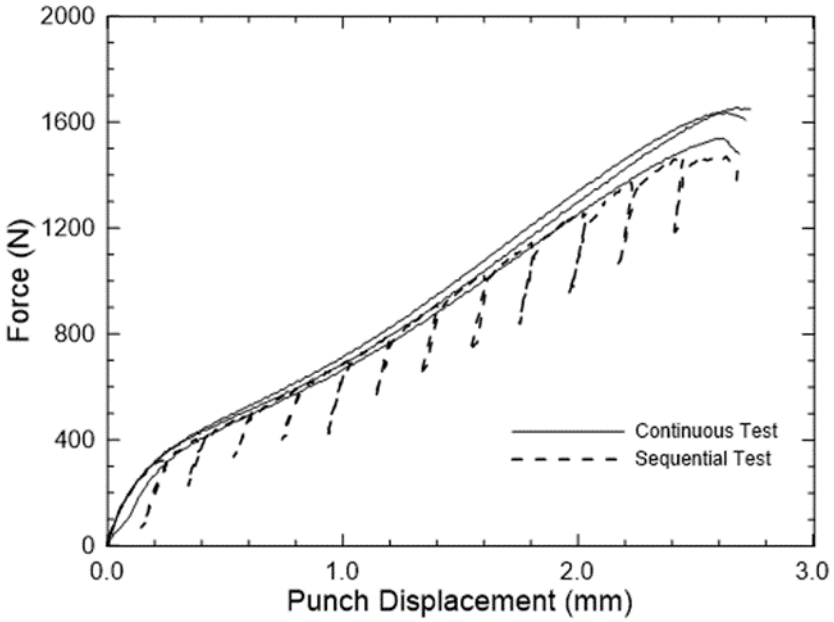

Figure 25. Punch force as a function of punch displacement in thin-backed experiments

Figure 26 shows the “Waterfall” plots of the maximum principal strain along the diameter line on the back surface of the specimen (the surface that is in contact with the copper plate) at four punch force values.

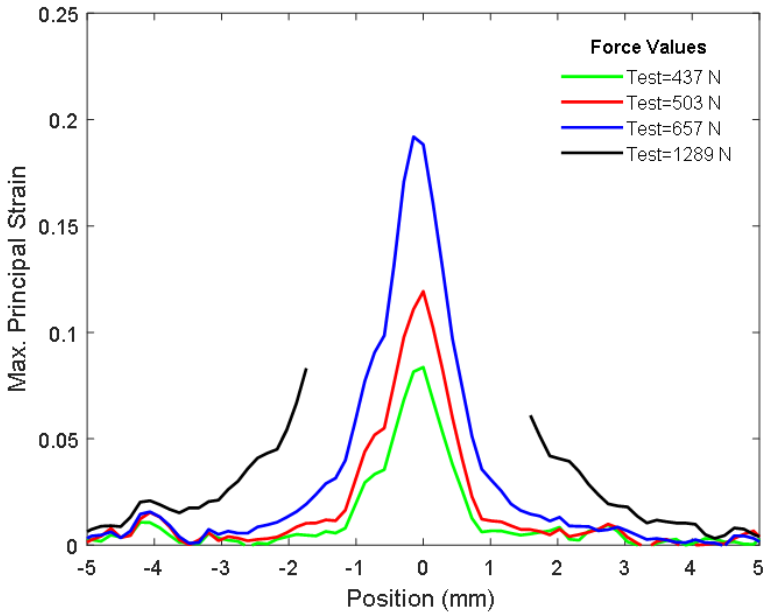

Figure 26. Maximum principal strain along the diameter line on the back surface of the specimen in a thin-backed plate test at different punch force values

Up to a punch force of about 660 N, strains are measured continuously along the diameter line. At larger forces the strain near the center of the punch could not be determined with DIC because the localized pressure at the interface between the back surface of the specimen plate and the copper backing plate and the relative displacement between the plates degrades the quality of the paint speckle pattern. At a punch force of about 1,280 N, strain from DIC is measureable only at distances larger than about 1.6 mm from the center. For this complex, 3D stress state, triaxiality and Lode parameter (and equivalent plastic failure strain) must be determined from numerical simulations and is determined separately (Park, Kelly, DuBois, Condasco, & Kan, 2020).

Results from the thick-backed plate tests are displayed in Figure 27 and Figure 28. Figure 27 shows measured punch force versus punch displacement curves from three tests where the specimen is loaded continuously up to fracture and one representative curve from an interrupted test where the

specimen is loaded in eleven sequential steps until fracture is observed. Fracture is observed at an average punch displacement of about 2.15 mm and average force of 2,400 N.

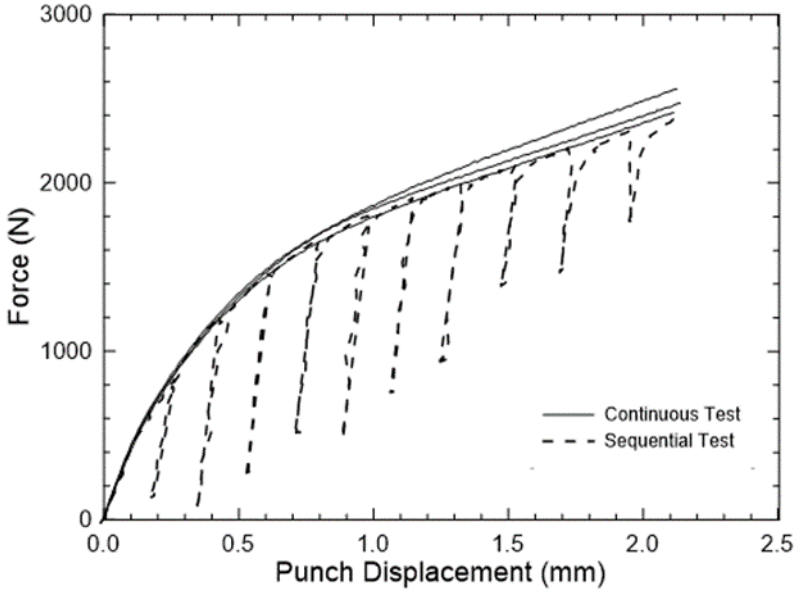

Figure 27. Punch force as a function of punch displacement in thick-backed experiment

Figure 28 shows the “Waterfall” plots of the maximum strain along the diameter line on the back surface of the specimen (the surface that is in contact with the copper plate) at four punch force values.

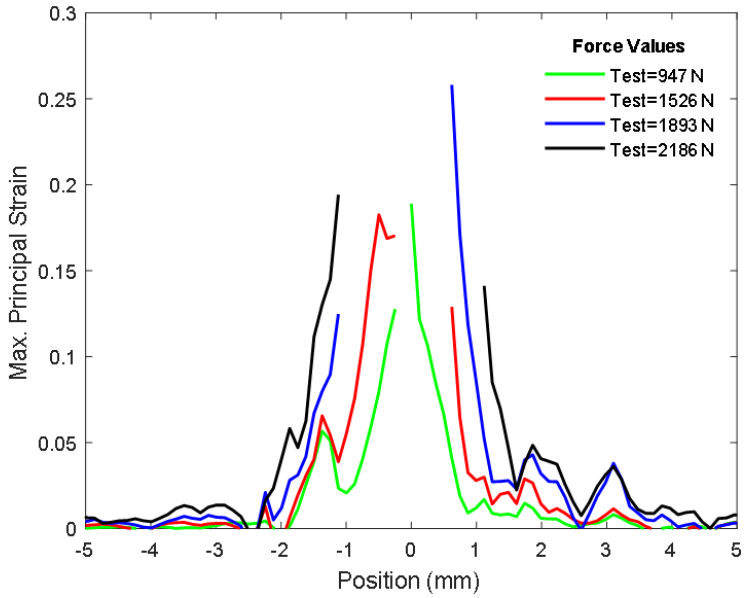

Figure 28. Maximum principal strain along the diameter line on the back surface of the specimen in a tick-backed test at different punch force values

At a punch force of about 950 N, strain is measured almost continuously along the line, however, at larger forces strains near the center-line of the punch could not be determined with DIC due to speckle pattern breakdown. The history of the calculated triaxiality, Lode parameter, and equivalent plastic strain at fracture is determined separately through parallel numerical simulations (Park, Kelly, DuBois, Condasco, & Kan, 2020).

Images of test specimens at the onset of fracture shown in Figure 29.

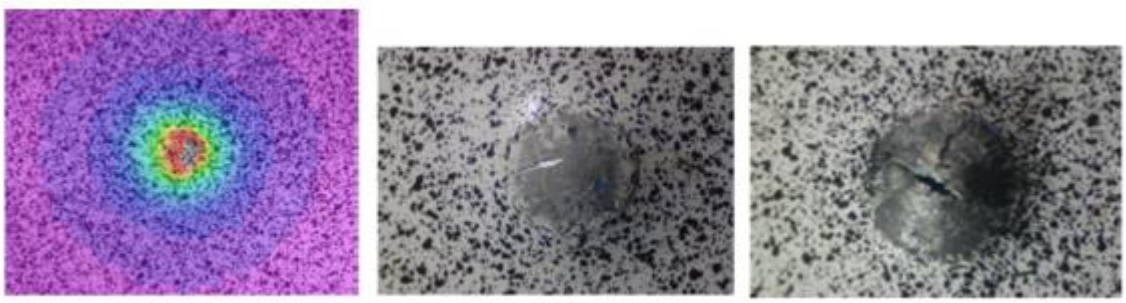

Figure 29. Fracture on the back surface of the specimens: (a) unbacked, (b) thin-backed, (c) thick-backed

A DIC maximum principal strain contour for an unbacked test is shown in Figure 29(a). Thin and thick backed specimens are shown in Figure 29(b) and (c), respectively. These two images were taken after the final loading increment of a sequential test. These images clearly show different deformation and fracture mechanisms for the three cases. Additional details can be found in (Spulak, 2020).

5 Summary and conclusions

5.1 Conversion of plastic work into heat for Aluminum 2024-T351 over a wide range of strain rates

This report describes additional tests conducted to study the conversion of plastic work into heat for 2024-T351 aluminum. The goal of this test series was to increase the accuracy of a *MAT_224 calibration for 0.5 in thick 2024-T351 aluminum for the FAA's ACFPP. A lack of temperature specimen data made it impossible to have confidence that the dynamic experiments were being modeled correctly because there was no way to know the fraction of plastic work converted to heat. A test series was devised to determine the fraction of plastic work converted to heat (or β_{int}). A series of tension tests were conducted at strain rates ranging from quasi-static (1E-4 s^{-1}) to 6000 s-1. Simultaneous full-field strain and temperature were measured using a high speed visible camera for DIC and a high speed IR camera, respectively. The visible and IR cameras were synchronized both temporally and spatially and full-field β_{int} was determined from superposed strain and temperature data sets. Average β_{int} for 2024-T351 aluminum ranges from 0.114 at a strain rate of 0.1 s^{-1} to ~ 0.5 at adiabatic conditions (strain rate greater than or equal to 500 s^{1}).

5.2 Compression torsion testing of thin-walled tube specimens

To supplement the previous axial-torsional fracture-strain test data, combined compression and torsion tests on thin-walled tube samples were conducted at a new (more compressive) axial stress to torsional stress ratio. Load frame control settings were used to achieve $\frac{\sigma_x}{\tau_{xy}}$ = ~-1.70.

Three tests were conducted and average equivalent strain at fracture of 0.71 was measured. This fracture strain is substantially higher than that observed at the nearest stress state (0.57 for LR4 compression torsion tests) and more than twice that of uniaxial tension (~0.3 for SG1 and SG5).

5.3 Fracture strain of Aluminum 2024-T351 under in-plane biaxial tension and out-of-plane compression

A small-diameter punch experiment of a specimen plate supported by a backing plate was successfully used to determine the equivalent plastic strain at fracture of a material element subjected to loading under a state of stress of biaxial in-plane tension and out-of-plane

compression. These data along with parallel numerical simulations allowed the determination of triaxiality and Lode parameter values throughout the test as well as the associated plastic strain. For the 2024-T351 aluminum, results were obtained at estimated triaxiality ranges from -0.652 to 0.113 (positive triaxiality for compression), and near constant Lode parameter of about -1. The values obtained for the fracture strain show a clear increase in failure strain with increasing triaxiality, or increasing compression. This was expected, as more compression tends to inhibit void and crack growth and propagation, and therefore inhibit ductile failure.

Data from this new punch experiment together with data from prior tests (tension of notched specimens, combined tension/compression-shear tests, etc.) in which ductile fracture was characterized under loading at other states of stress is essential for the calibration of new continuum ductile fracture models for impact scenarios.

6 References

ASTM. (2009). E643-09. *Standard Test Method for Ball Punch Deformation of Metallic Sheet Metals*. West Conshohocken, PA: ASTM International.

Bao, Y. (2003). Prediction of ductile crack formation in uncracked bodies. *Ph.D. Thesis*. Massachusetts Institute of Technology.

Bao, Y., & Wierzbicki, T. (2004). On fracture locus in the equivalent strain and stress triaxiality space. *International Journal of Mechanical Sciences, 46*, 81-98.

Bao, Y., & Wierzbicki, T. (2010). Application of extended Mohr–Coulomb criterion to ductile fracture. *161*, 1-20.

Barsoum, I., & Faleskog, J. (2007). Rupture mechanisms in combined tension and shear-Experiments. *International Journal of Solids and Structures, 44*, 1768-1786.

Bever, M., Holt, D., & Titchner, L. (1973). The stored energy of cold work. *Prog. Mater. Sci., 17*, 5-177.

Børvik, T., Hopperstad, O. S., & Berstad, T. (2003). On the influence of stress triaxiality and strain rate on the behaviour of a structural steel. Part II. Numerical study. *European Journal of Mechanics A/Solids, 22*, 15-32.

Buyuk, M. (2014). Development of a new metal material model in LS-DYNA Part 1: Development of a tabulated thermo-viscoplastic material model with regularized failure for dynamic ductile failure prediction of structures under impact loading [DOT/FAA/TC-13/25]. Federal Aviation Administration. Retrieved from https://www.tc.faa.gov/its/worldpac/techrpt/tc13-25p2.pdf

Charkaluk, E., Seghir, R., Bodelot, L., Witz, J.-F., & Dufrénoy, P. (2015). Microplasticity in polycrystals: A thermomechanical experimental perspective. *Experimental Mechanics, 55*(4), 741-752.

Del Campo, L., Pérez-Sáez, R. B., González-Fernández, L., Esquisabel, X., Fernández, I., González-Martín, P., & & Tello, M. J. (2010). Emissivity measurements on aeronautical alloy. *Journal of Alloys and Compounds, 489*(2), 482-487.

Dumoulin, S., Louche, H., Hopperstad, O. S., & Børvik, T. (2010). Heat sources, energy storage and dissipation in high-strength steels: Experiments and modelling. *European Journal of Mechanics-A/Solids, 29*(3), 461-474.

Eisenlohr, A., Gutierrez-Urrutia, I., & Raabe, D. (2012). Adiabatic temperature increase associated with deformation twinning and dislocation plasticity. *Acta materialia, 60*(9), 3994-4004.

Emmerling, W., Altobelli, D., Carney, K., & Pereira, M. (2014). Development of a new metal material model in LS-DYNA Part 1: FAA, NASA, and industry collaboration background [DOT/FAA/TC-13/25]. Federal Aviation Administration.

Farren, W., & Taylor, G.I. (1925). The heat developed during plastic extension of metals. *Proc. R. Soc. London A, 107*, 422-451. doi:https://doi.org/10.1098/rspa.1925.0034

Gao, X., & Kim, J. (2006). Modeling of ductile fracture: Significance of void coalescence. *International Journal of Solids and Structures, 43*, 6277-6293.

Hancock, J., & Mackenzie, A. (1976). On the mechanisms of ductile failure in high-strength steels subjected to multi-axial stress-states. *Journal of the Mechanics of Physical Solids, 24*, 147-169.

Hodowany, J., & Ravichandran, G. (2000). Partition of plastic work into heat and stored energy in metals. *Experimental Mechanics, 40*, 113-123.

Hopperstad, O. S., Børvik, T., Langseth, M., Labibes, K., & Albertini, C. (2003). On the influence of stress triaxiality and strain rate on the behaviour of a structural steel. Part I Experiments. *European Journal of Mechanics A/Solids, 22*, 1-13.

Johnson, G. R., & Cook, W. H. (1983). A constitutive model and data for metals subjected to large strains, high strain rates and high temperatures. *Proc. 7th Inf. Sympo. Ballistics*, (pp. 541-547). The Hague.

Johnson, G. R., & Cook, W. H. (1985). Fracture characteristics of three metals subjected to various strains, strain rates, temperatures, and pressures. *Engineering Fracture Mechanics, 21*, 31-48.

Knysh, P., & Korkolis, Y. P. (2015). Determination of the fraction of plastic work converted into heat in metals. *Mechanics of materials, 86*, 71-80.

Labuz, J., & Zang, A. (2012). Mohr-Coulomb failure criterion. *Rock Mechanics and Rock Engineering, 45*, 975-979.

Macdougall, D. A. (2000). Determination of the plastic work converted to heat using radiometry. *Experimental Mechanics, 40*(3), 298-306.

Macdougall, D. A., & Harding, J. (1998). The measurement of specimen surface temperature in high-speed tension and torsion tests. *International Journal of Impact Engineering, 21*(6), 473-488.

Mackenzie, A., Hancock, J., & Brown, D. (1977). On the influence of state of stress on ductile failure initiation in high strength steels. *Engineering Fracture Mechanics, 9*, 167-188.

Mason, J., Rosakis, A., & Ravichandran, G. (1994). On the strain and strain rate dependence of the fraction of plastic work converted to heat: an experimental study using high speed infrared detectors and the Kolsky bar 1. *Mech. Mater.,, 17*, 135-145.

Mohr, D., & Henn, S. (2007). Calibration of stress-triaxiality dependent crack formation criteria: A new hybrid experimental-numerical method. *Experimental Mechanics, 47*, 805-820.

Mohr, D., & Marcadet, S. (2015). Micromechanically-motivated phenomenological Hosford–Coulomb model for predicting ductile fracture initiation at low stress triaxialities. *International Journal of Solids and Structures, 67*, 40-55.

Nemat-nasser, S., & Kapoor, R. (1998). Determination of temperature rise during high strain rate deformation. *Mechanics of Materials, 27*, 1-12.

Oliferuk, W., Maj, M., & Zembrzycki, a. K. (2015). Determination of the energy storage rate distribution in the area of strain localization using infrared and visible imaging. *Experimental Mechanics, 55*(4), 753-760.

Park, C. K., Kelly, C., DuBois, P., Condasco, D., & Kan, C. D. (2020). Aluminum 2024-T351 input parameters for MAT_224 in LS-DYNA [DOT/FAA/TC-19/41]. Federal Aviation Administration.

Quinney, H., & Taylor, G. (1934). The latent energy remaining in a metal after cold working. *Proc. R. Soc. London, A 143*(849), 307-326.

Rice, J., & Tracey, D. (1969). On the ductile enlargement of voids in triaxial stress fields. *Journal of the Mechanics and Physics of Solids, 17*, 201-217.

Rittel, D. (1999). On the conversion of plastic work to heat during high strain rate deformation of glassy polymers. *Mechanics of Materials, 31*(2), 131-139.

Rittel, D., Zhang, L. H., & Osovski, S. (2017). The dependence of the Taylor–Quinney coefficient on the dynamic loading mode. *Journal of the Mechanics and Physics of Solids, 107*, 96-114.

Rodríguez-Martínez, J. A., Pesci, R., & Rusinek, A. (2011). Experimental study on the martensitic transformation in AISI 304 steel sheets subjected to tension under wide ranges of strain rate at room temperature. *Materials Science and Engineering: A, 528*(18), 5974-5982.

Saai, A., Louche, H., Tabourot, L., & Chang, H. J. (2010). Experimental and numerical study of the thermo-mechanical behavior of Al bi-crystal in tension using full field measurements and micromechanical modeling. *Mechanics of Materials, 42*(3), 275-592.

Seidt, J. (2010). Plastic deformation and ductile fracture of 2024-T351 Aluminum under various loading conditions. [Doctoral dissertation, Department of Mechanical Engineering, The Ohio State University].

Seidt, J. (2014). P3 Development of a new material model in LS-DYNA – Part 3: Plastic deformation and ductile fracture of 2024 aluminum under various loading conditions [DOT/FAA/TC-13/25]. Federal Aviation Administration.

Seidt, J., Pereira, J., & Gilat, A. (2015). Influence of fabrication method on tensile response of split-Hopkinson bar-sized specimens. *Journal of Testing and Evaluation, 43*(6), 1563-1573.

Smith, J. (2019). Full-field measurement of the Taylor-Quinney coefficient in tension tests of Ti-6Al-4V, Aluminum 2024-T351, and Inconel 718 at various strain rates. [Doctoral dissertation, Department of Mechanical Engineering, The Ohio State University].

Spulak, N. L. (2020). Ductile fracture under in-plane biaxial tension and out-of-plane compression. *International Journal of Solids and Structures, 202*, 234-242.

Staab, G. G. (1991). A direct-tension split Hopkinson bar for high strain rate testing. *Experimental Mechanics, 31*, 232-235.

Xue, L. (2007). Damage accumulation and fracture initiation in uncracked ductile solids subject to triaxial loading. *International Journal of Solids and Structures, 44*, 5163-5181.

Yagoubi, J. E., Lamon, J., Batsale, J.-C., Dhote, J., & Flem, M. L. (2015). Multiscale thermal characterization of mechanically loaded ceramic matrix composite: Estimation of thermal diffusivity at micro/mesoscale. *Experimental Mechanics, 55*(4), 783-794.

Zehnder, A., & Rosakis, A. (1991). On the temperature distribution at the vicinity of dynamically propagating cracks in 4340 steel. *J. Mech. Phys. Solids, 39*(3), 385-415.

Zhang, K., Bai, J., & Francois, D. (2001). Numerical analysis of the influence of the Lode parameter on void growth. *International Journal of Solids and Structures, 38*, 5847-5856.